

## FULL POLAR CAP CASCADE SCENARIO: $\gamma$ -RAY AND X-RAY LUMINOSITIES FROM SPIN-POWERED PULSARS

BING ZHANG<sup>1</sup> AND ALICE K. HARDING

Laboratory of High Energy Astrophysics, NASA/Goddard Space Flight Center, Greenbelt, MD 20771  
bzhang@twinkie.gsfc.nasa.gov, harding@twinkie.gsfc.nasa.gov

*final version, to appear in ApJ*

### ABSTRACT

Canonical polar cap cascade models involve curvature radiation (CR) or inverse Compton scattering (ICS) of the primary particles and synchrotron radiation (SR) of the higher generation pairs. Here we modify such a cascade picture to include the ICS of the higher generation pairs. In such a “full-cascade” scenario, not only the perpendicular portion of the energy of the pairs goes to high energy radiation via SR, but the parallel portion of the energy of the pairs can also contribute to high energy emission via ICS with the soft thermal photons from either the full neutron star surface or the hot polar cap. The efficiency of converting particles’ kinetic energy to radiation by ICS is very high if the scatterings occur in the “resonant” regime. As a result, almost 100% of the energy input from the pulsar inner accelerators could be converted to high energy emission. An important output of such a scenario is that the soft tail of the ICS spectrum can naturally result in a non-thermal X-ray component which can contribute to the luminosities observed by ROSAT and ASCA.

Here we present an analytic description of such a full polar cap cascade scenario using the recursion relationships between adjacent generations following the approach first proposed by Lu et al. (1994), but develop it to be able to delineate the complex full-cascade process. The acceleration model we adopted is the space-charge-limited flow model proposed by Harding & Muslimov (1998). We present the theoretical predictions of the  $\gamma$ -ray luminosities, the thermal and non-thermal X-ray luminosities for the known spin-powered X-ray pulsars (8 of them are also  $\gamma$ -ray pulsars), and compare them with the observations from CGRO, ROSAT and ASCA. We estimate the non-thermal X-ray luminosity by including all the possible ICS branches contributing to a certain energy band, and estimate both the full surface and hot polar cap thermal X-ray luminosities by adopting a standard neutron star cooling scenario, and by treating self-consistent polar cap heating in the Harding & Muslimov (1998) model, respectively. Our results show that the observed different dependences of the high energy luminosities on the pulsar spin-down luminosities, i.e.,  $L_\gamma \propto (L_{sd})^{1/2}$  and  $L_x \sim 10^{-3}L_{sd}$ , are well reproduced. We found that, for normal pulsars, both the hard (ASCA band) and the soft (ROSAT band) X-ray luminosities are dominated by the non-thermal X-rays of ICS origin, although for some pulsars, thermal components due to either neutron star cooling or polar cap heating can have comparable luminosities so that they are detectable. For the millisecond pulsars, our predicted upper limits of the thermal luminosities due to polar cap heating are usually higher than the ICS-origin non-thermal components if there are no strong multipolar magnetic field components near the neutron star surface, thus the *pulsed* soft X-rays in the ROSAT band from most of the millisecond pulsars might be of thermal origin.

*Subject headings:* pulsar: general - radiation mechanism: non-thermal - X-rays: stars

### 1. INTRODUCTION

Among about 1000 spin-powered radio pulsars detected so far, 35 are detected as X-ray sources with 11 of them being X-ray pulsars (for recent reviews, see Becker & Trümper 1997, update version 1999, hereafter BT97; Saito 1998, hereafter S98; Saito et al. 1997), and at least 8 are detected also as  $\gamma$ -ray pulsars (for recent reviews, see Thompson et al. 1997; Thompson et al. 1999. The eighth one, PSR 1046-58, was recently reported by Kaspi et al. (1999)). Though detailed data for these spin-powered high energy pulsars are still poor, and some of them even have a great diversity of emission features, there do exist some empirical laws. One prominent feature is the dependence of the observed high energy luminosities on the pulsar spin-down luminosities: For  $\gamma$ -rays, it is found that  $L_\gamma \propto (L_{sd})^{1/2} \propto B/P^2$  (Thompson et al. 1997); while for X-

rays, the dependence of  $L_x(ROSAT) \sim 10^{-3}L_{sd} \propto B^2/P^4$  is found in ROSAT (0.1-2.4 keV) data (BT97). A rough dependence of  $L_x(ASCA) \propto (L_{sd})^{3/2} \propto B^3/P^6$  for ASCA (0.7-10 keV) data is reported by Saito (1998, hereafter S98) and Saito et al. (1997) based on a relatively smaller sample than the ROSAT data. However, in view of the large uncertainties such as unknown beaming, hydrogen column density, distance, assumptions of spectral shape, instrument response, calibration uncertainties, and so on, the ASCA data are not inconsistent to the ROSAT data.

Combining the ROSAT and ASCA data, spectral analysis of some of the X-ray pulsars are available. Full-surface thermal emission components are identified from four pulsars, i.e., Vela (Ögelman, Finley & Zimmermann 1993), Geminga (Halpern & Wang 1997), PSR 0656 +14 and PSR 1055-52 (Greiveldinger et al. 1996; Wang et al. 1998), usually accompanied by a hard non-thermal compo-

<sup>1</sup>National Research Council Research Associate Fellow.

ment. As for the small-area hot thermal components, the evidence is not robust. Geminga (Halpern & Ruderman 1993), PSR 0656+14 and PSR 1055-52 (Greiveldinger et al. 1996) have been reported to show such components, but follow-up data analyses show that the hard components are more likely power-law (Halpern & Wang 1997; Wang et al. 1998). Two nearby old pulsars, PSR 1929+10 and PSR 0950+19 are reported to be dominated by a single small-area hard thermal component (Wang & Halpern 1997), but such conclusions are also not solid, since PSR 1929+10 could be equally well fitted by a single power law (BT97), and the measurements of PSR 0950+19 reported by Wang & Halpern (1997) are heavily contaminated by another source in the ASCA field of view (S98). For the millisecond pulsar PSR J0437-4715, two-component spectral fits using the ROSAT plus EUVE data require a hot small-area thermal component (Becker & Trümper 1993; Halpern, Martin & Marshall 1996; Zavlin & Pavlov 1998), although a simple power-law (BT97) or a broken power-law (Becker, Trümper 1999) fit is also acceptable. Among others, 7 ROSAT (BT97) and 1 ASCA (S98) pulsars are identified to show power-law spectral features, which suggests a non-thermal origin. The detected X-ray photons from the rest of pulsars are too few for spectral fits, but they are commonly thought to be of non-thermal origin as well, due to the close relationships of their X-ray luminosities to the spin-down luminosities (e.g. BT97; S98).

Two general classes of models have been proposed for high-energy pulsars. The polar cap models (Harding 1981; Daugherty & Harding 1982; 1994; 1996, hereafter DH96; Sturmer & Dermer 1994; Sturmer, Dermer & Michel 1995, hereafter SDM95) interpret pulsar high energy emission as curvature radiation (CR) or magnetic inverse Compton scattering (ICS) induced pair production cascade in the polar cap region; while the outer gap models (e.g. Cheng, Ho & Ruderman 1986a,b; Romani & Yadigaroglu 1995; Romani 1996; Zhang & Cheng 1997) interpret pulsar high energy emission as fan beam radiation originating in the large vacuum gaps in the outer magnetosphere beyond the null charge surface. In the early polar cap cascade pictures, the observed  $\gamma$ -emission is interpreted as the primary CR and the synchrotron radiation (SR) from the higher generation pairs (Daugherty & Harding 1982, 1994, 1996; Zhao et al. 1989; Lu & Shi 1990; Lu, Wei & Song 1994 hereafter LWS94; Wei, Song & Lu 1997, hereafter WSL97). Recently, the importance of the ICS with the soft thermal photons from the NS surface by the primary particles is noticed. It is found that ICS is not only a significant energy loss (Kardashëv et al. 1984; Xia et al. 1985; Daugherty & Harding 1989; Sturmer 1995) mechanism, but is also a mechanism of  $\gamma$ -ray emission (Sturmer & Dermer 1994; SDM95) and to ignite pair-production cascades (Zhang & Qiao 1996; Zhang et al. 1997a,b). However, Harding & Muslimov (1998, hereafter HM98) argued that the asymmetry of upward versus downward ICS induced pair cascades make a ICS-controlled accelerator usually unstable near the stellar surface in the space-charge-limited flow acceleration model, so that a CR-controlled accelerator could be stabilized at a height of 0.5-1 stellar radii above the NS surface when the energy loss efficiency of ICS is less than that of CR. As a result, the CR-induced cascades

picture (DH96) could still be maintained, although ICS of the primaries will also contribute to the final  $\gamma$ -ray spectrum. The high-altitude accelerator naturally matches the extended polar cap cascade model (DH96).

In such a polar cap model, it is predicted that there is a low-energy turnover at the blueshifted local cyclotron frequency in the high energy spectra of pulsars (Harding & Daugherty 1999). Such a feature is also noticed by Rudak & Dyks (1999) who argued that the non-thermal X-rays observed by ROSAT and ASCA pose a challenge to such a model, and it could be a discriminator between the rivaling classes of models, since the dependence of  $L_x \sim 10^{-3} L_{sd}$  could be interpreted in terms of a thick outer gap model (Cheng, Gil & Zhang 1998, hereafter CGZ98; Cheng & Zhang 1999, hereafter CZ99). However, there is yet another important point which has been overlooked in previous studies of polar cap cascade scenarios. This is the possible contributions of the ICS photons produced by higher generation pairs to the pulsar high energy radiation. Even in the ICS-induced polar cap cascade model (SDM95), these contributions were not included, since the authors found that these ICS photons are not energetic enough to pair-produce again<sup>2</sup>, though they admitted that most of these scatterings occur in the “resonant” regime so that they should be important for spectral formation. Here we will improve the polar cap cascade picture by including the ICS contributions of the higher generation pairs. We will adopt an analytic approach to describe such a more complicated “full-cascade” process and examine how significant these contributions are. A straightforward conclusion is that, the low energy tail of such ICS spectra can naturally provide a non-thermal X-ray component, which could contribute to the ROSAT and ASCA bands observations. We will show that, the full cascade model combined with the HM98 acceleration model can not only present a clear  $L_\gamma \propto (L_{sd})^{1/2}$  feature, but the ICS-origin non-thermal X-ray components with the combination of the thermal components due to polar cap heating can also reproduce the rough  $L_x \sim 10^{-3} L_{sd}$  dependence. The preliminary results of this study is shown in Zhang & Harding (1999).

The organization of this paper is as follows. In Sect. 2.1-2.4, we describe in detail the analytic approach to delineate the cascade processes. Such descriptions are independent of the acceleration model and thus could be used in any model when the inner accelerator (gap) features are specified. Sect. 2.5 reviews the main features of the acceleration model proposed by Harding & Muslimov (HM98), which has incorporated the frame-dragging-induced parallel electric fields and both the CR- and ICS- induced cascade processes, and therefore is hitherto the most complete space-charge-limited flow acceleration model. In Sect. 3.1-3.4, we explicitly present our model predictions of the total high energy luminosities (mainly the  $\gamma$ -ray luminosities), thermal, and non-thermal X-ray luminosities from the known pulsars, and compare them with the observations from CGRO, ROSAT and ASCA. Our main results are summarized in Sect.4 with some discussions.

<sup>2</sup>This is true for most of pulsars, but is not the case for the pulsars with high magnetic fields. See our calculation results presented in Table 2 and corresponding discussions.

## 2. THE MODEL

## 2.1. Resonant scattering condition and the “full-cascade” picture

In our work, it is assumed that there exist two thermal emission components from neutron stars: one soft component over the whole surface with the temperature  $T_s$ , and a hot component at the polar cap region with the temperature  $T_h$ . As reviewed in the previous section, these components have actually been detected from some pulsars (though with some uncertainties), and they are commonly expected by various theories. The full surface radiation is predicted in various neutron star cooling (e.g. Van Riper & Lamb 1981; Nomoto & Tsuruta 1987) and internal heating (e.g. Alpar et al. 1984; Shibazaki & Lamb 1989; Schaab et al. 1999) models. In the outer gap heating models, it is supposed that the hard X-rays emitted from the hot polar cap may be reflected back to the surface by a “pair-blanket” due to the magnetic cyclotron resonant absorption, so that they might be reemitted from the full neutron star surface with softer energies (Halpern & Ruderman 1993; Zhang & Cheng 1997; Wang et al. 1998; CGZ98; CZ99). A hotter polar cap is expected by either polar cap heating (e.g. Arons 1981; Harding, Ozernoy & Usov 1993; Muslimov & Tsygan 1992; HM98) or outer gap heating (again Halpern & Ruderman 1993, etc.). The ICS of the relativistic particles with these thermal photons is the main topic discussed in this paper. Thus our present model is solely contingent upon the existence of the thermal photon fields in the neutron star vicinity, and can not be justified if it turns out that there is no such thermal emission at all. Note there should be also some ICS processes with the soft non-thermal X-rays if they do exist, and such processes will not be discussed in this paper.

The so called “resonant scattering condition” (Daugherty & Harding 1989; Dermer 1990) is essential in our “full-cascade” picture. This condition ensures that the bulk of the soft thermal photons near the neutron star surface with peak energy  $2.82kT = 0.24T_6(\text{keV})$  could be Lorentz-boosted to the particle’s rest-frame local field cyclotron energy  $\hbar\omega_B = \hbar eB_e/mc = 11.6B_{e,12}(\text{keV})$ , where  $B_e$  is the magnetic field strength at the emission (scattering) point. More specifically, this condition reads  $\gamma(1 - \beta\mu) \cdot 2.82kT \gtrsim \hbar\omega_B$ , or

$$\gamma \gtrsim \gamma_{\text{res}} = \frac{48B_{12}}{[(1 - \beta\mu)T_6]}, \quad (1)$$

where  $\mu = \cos\theta$  is the cosine of the incident angle of the scattering, and  $\gamma$  is the Lorentz factor of the electron. For the case of actual pulsars with two thermal components, we adopt different geometries with

$$\mu_{s,\text{max}} = (1 - r_{e,6}^{-2})^{1/2} \quad (2)$$

for the soft full-surface component, and

$$\mu_{h,\text{max}} = \text{Max} \left[ \frac{r_{e,6} - 1}{\left[ (r_{e,6} - 1)^2 + \left( \frac{\Omega R}{c} \right)^{1/2} \right]^{1/2}}, (1 - r_{e,6}^{-2})^{1/2} \right] \quad (3)$$

for the hot polar cap component, where  $r_{e,6}$  is the radius of the emission point in units of  $10^6\text{cm}$  (i.e. the stellar

radius). Note that the two terms on the right hand of (3) are for different emission height regimes, the conjunction of which is the height above which the horizon of the emission point is greater than the polar cap area. Then the resonant condition (1) becomes

$$\gamma \gtrsim \gamma_{\text{res}} = \frac{48B_{12}}{\text{Max}[(1 - \beta\mu_{s,\text{max}})T_{s,6}, (1 - \beta\mu_{h,\text{max}})T_{h,6}]}. \quad (4)$$

In the resonant ICS regime, the e-folding mean free path of the particles with Lorentz factor  $\gamma$  (Dermer 1990; Sturmer 1995)

$$\lambda_{\text{res}} \simeq -0.061(\text{cm})\gamma^2 T_6^{-1} B_{e,12}^{-2} \times \ln^{-1} \left[ 1 - \exp \left( -\frac{134B_{e,12}}{\gamma T_6(1 - \beta\mu)} \right) \right], \quad (5)$$

is very small due to the tremendous enhancement of the scattering cross section near the resonant frequency, so that the particles could efficiently convert their kinetic energies into radiation before moving a long distance. Thus, as long as the condition (4) is satisfied, the Lorentz factor of the particles will keep decreasing all the way down to the value when the condition (4) fails. Then, most of the kinetic energies of the particles are converted to radiation.

According to Dermer (1990) and Sturmer (1995), there is a wide regime of the Lorentz factors of the particles which satisfies the resonant condition (4). The resonant scattering takes place not only for the primary particles within the accelerator, but also for the secondary pairs produced above the accelerator. Zhang et al. (1997b) have calculated the Lorentz factor evolution above the gap for the secondary pairs within the framework of the Ruderman-Sutherland (1975, hereafter RS75) type vacuum gap acceleration model. They found that the resonant ICS process can reduce the energies of the secondary pairs to much lower values than the original ones, which may constrain pulsar radio emission frequency to below a certain value. However, they did not consider the contribution of these energies to the high energy radiation of the pulsars. In fact, such secondary ICS processes will also produce high energy emission which contributes to the final spectra of the  $\gamma$ -ray pulsars. The low frequency tail of such spectra can contribute to a non-thermal X-ray emission component. As a result, it is important to modify the conventional CR(or ICS)-SR polar cap model to include this ICS effect.

We then come to a “full-cascade picture” (Fig.1): the primary particles within the accelerator emit primary  $\gamma$ -rays, which produce secondary pairs via  $\gamma$ - $B$  process. The perpendicular energies of these secondary pairs are rapidly converted to radiation via SR, while most of the parallel energies will also be converted to radiation via ICS if the resonant scattering condition (4) is satisfied. Thus two-branch secondary generation  $\gamma$ -rays are produced. These secondary  $\gamma$ -rays may undergo the  $\gamma$ - $B$  process again to produce higher two-branch generation pairs and  $\gamma$ -rays. Such processes go on and on until the  $\gamma$ -rays escape from the magnetosphere.

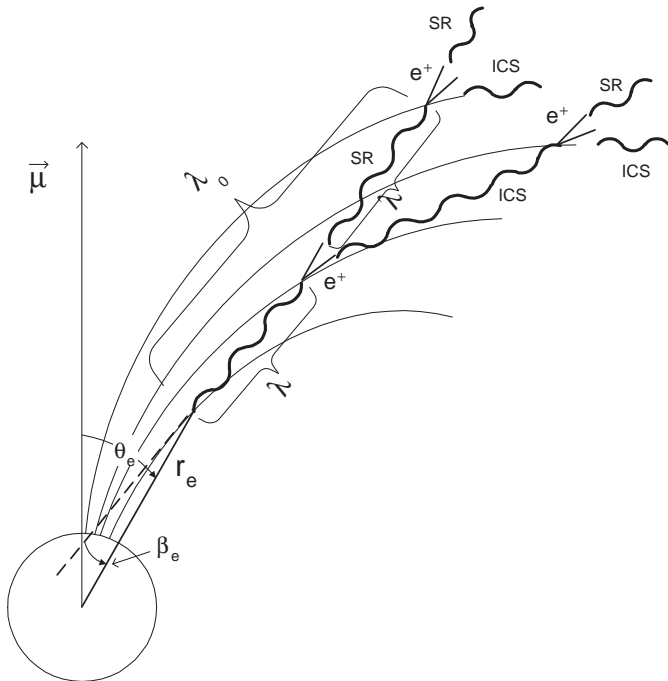


FIG. 1.— A Schematic illustration of the full cascade process. The coordinates of the emission point are  $(r_e, \theta_e)$ , and  $\beta_e$  is the angle between the radial and tangential directions at the emission point. The wavy lines denote the photons. SR-branch photons follow the original direction of the pairs, while ICS-branch photons follow the tangential direction.  $l$  is the attenuation length of each generation photon, and  $l_0$  is scaled from the original emission point where the photon is emitted tangentially.

In this paper, we will limit ourselves to an analytic approach to understand the complex “full cascade” processes. An analytic method (e.g. LWS94; WSL97) is helpful to present an over-all picture for the pulsar population, and can, to some extent, predict some features of the numerical results.

We have some remarks on the validity of condition (4) for millisecond pulsars. Since the cyclotron energies in millisecond pulsars are much lower than the thermal peak energies, very small incident angles (e.g.  $\mu \sim 1$ ) are required to keep the thermal photons Lorentz-down-boosted to the cyclotron frequency, and we can get an absolute upper limit of Lorentz factors of the particles for resonant scattering by adopting  $\mu = 1$ . Noticing  $1 - \beta \simeq 1/2\gamma^2$ , this turns out

$$\gamma \leq 105T_6/B_8. \quad (6)$$

When this condition fails, as long as condition (4) is satisfied, there are still some off-peak thermal photons which are resonantly scattered, but the energy conversion efficiency is much lower due to the smaller “soft” photon numbers. Even if both (4) and (6) are satisfied, the mean free path of resonant scattering (5) is still much longer than the normal pulsars due to the tremendous decrease of the field strength. Thus ICS energy conversion efficiency is low for millisecond pulsars. As shown later in Sect.3.3, for the millisecond pulsars, usually the non-thermal soft X-

rays of ICS-origin are dominated by the polar-cap-heating-produced thermal X-rays.

## 2.2. $\gamma - B$ pair production and photon escaping energy

The one-photon pair production process or the  $\gamma - B$  process plays an essential role in the polar cap cascade scenario. A detailed description of the process and explicit numerical computations were presented in Harding, Baring & Gonthier (1997, hereafter HBG97). Here we will adopt some approximations within certain reasonable regimes and come to some analytic expressions.

### 2.2.1. Attenuation mean free path

We adopt the simple asymptotic formula of Erber (1966). Assuming that the one photon attenuation coefficient is constant over the distance interested in, we get the mean free path of attenuation, which is simply the inverse of the attenuation coefficient (e.g. RS75)

$$l = \frac{4.4}{(e^2/\hbar c)} \frac{\hbar}{mc} \frac{B_c}{B_\perp} \exp\left(\frac{4}{3\chi}\right)$$

or

$$l_6 = 1.03B_\perp^{-1} \exp\left(\frac{4}{3\chi}\right), \quad (7)$$

where

$$\chi = \frac{1}{2} \frac{E_\gamma}{mc^2} \frac{B_\perp}{B_c} = \frac{1}{2} \epsilon_\gamma B'_\perp, \quad (8)$$

and  $B_c = m^2 c^3 / e \hbar = 4.414 \times 10^{13}$  is the critical magnetic field,  $B'_\perp = B_\perp / B_c$ ,  $B_\perp = B \sin \theta_{\text{kB}}$ ,  $E_\gamma$  is the energy of the  $\gamma$ -photon in the local rest inertia frame, which should be corrected by a redshift factor (see eq.[86]) when compared with the observations,  $\epsilon_\gamma$  is  $E_\gamma$  normalized by  $mc^2$ , and  $\theta_{\text{kB}}$  is the angle between the photon and the field directions. Such an asymptotic formula is accurate enough when  $B' = B/B_c \leq 0.1$  (Daugherty & Harding 1983), which is the case for most pulsars in the HM98 model since the accelerators have been lifted to higher altitudes where strength of the local magnetic fields have dropped nearly an order of magnitude with respect to the surface fields (see Sect.2.5). But we should bear in mind that the asymptotic formula is unreliable at near threshold regime ( $\epsilon_\gamma \sin \theta_{\text{kB}} \gtrsim 2$ ), and should be modified to a more accurate asymptotic form (Daugherty & Harding 1983)

$$l_6 = 1.03B_\perp^{-1} \exp\left[\frac{4}{3\chi}(1 + \delta)\right] \quad (9)$$

with  $\delta = 0.42(\epsilon_\gamma/2 \sin \theta_{\text{kB}})^{-2.7} B'^{-0.0038}$ , or even no asymptotic formula at all (HBG97).

### 2.2.2. Geometric relations

The importance of general relativistic effects on one-photon pair production attenuation in a Schwarzschild metric has been examined by Gonthier & Harding (1994, hereafter GH94) and HBG97. They found that curved spacetime effects may influence the process in three ways, namely 1) curvature of the photon trajectories, 2) the redshift of the photon energy, and 3) the change in the dipole magnetic field (the shape of the field configuration and the enhancement of the field strength). Their conclusion

is that the distortion of the dipole in curved spacetime is compensated by the curved photon trajectory effect, but the increasing of the field strength in curved space-time will enhance the  $\gamma - B$  absorption and hence, lower the escaping photon energy. The relative redshifts of the photon energies between different generations are not large since the height differences between different generations are usually much smaller than one stellar radius. However, the redshift effect should be taken into account when comparing the calculated frequencies (in the local inertia frame) with the observational frequencies (the observers are located at infinity) (see eq.[86]). In our analytic study below, we will keep the flat spacetime geometry, i.e. assuming strict dipolar field configuration and straight trajectories of photon propagation. Neither of these assumptions are precise enough, but a combination of the two comes to a good approximation (GH94). We only incorporate an enhancement factor of the field strength due to curved spacetime (see eq.[19]). The redshift effect is only taken into account when comparing theoretical results with the observations (see eq.[86]).

In an exact “dipole” field in flat space-time, suppose a particle at  $(r_e, \theta_e)$  emits a photon along the field line, then there is a pure geometric relation between the perpendicular field strength the photon encounters, i.e.  $B_\perp$ , and the travel distance of the photon  $l$  (Hardee 1977)

$$B_\perp = \frac{3}{4} B_p R^3 \left[ \frac{l \sin \theta_e}{(r_e^2 + 2r_e l \cos \beta_e + l^2)^{5/2}} \right] \times [r_e (1 + \sin^2 \beta_e) + l \cos \beta_e], \quad (10)$$

where  $\beta_e$  is the angle between the field direction and the radial direction of the emission point, with  $\tan \beta_e = 1/2 \tan \theta_e$  (see Fig.1). Note  $B_p R^3/2$  (rather than  $B_p R^3$ ) is the dipole magnetic moment of a uniformly magnetized sphere of radius  $R$  (Usov & Melrose 1995; HBG97), so that  $B_p$  is identical to the surface magnetic field  $B_s$ , and is connected with pulsar period  $P$  and period derivative  $\dot{P}$  by

$$B_p = 6.4 \times 10^{19} \text{G} (P\dot{P})^{1/2}, \quad (11)$$

which is twice of the value adopted by Manchester & Taylor (1977) and Michel (1991).

Near the polar cap region, one has  $\theta_e \ll 1$ , and equation (10) becomes

$$B_\perp \simeq \frac{3}{4} B_p R^3 \frac{l \theta_e}{r_a^4} = \frac{3}{4} B_a \theta_e \frac{l}{r_a}, \quad (12)$$

where subscript “a” indicates the “absorption point”, so that  $r_a \simeq r_e + l$  and  $B_a = B_p \left(\frac{R}{r_a}\right)^3$ . Such a  $B_\perp$  has a maximum when  $l \simeq r_e/3$  (Hardee 1977), with

$$B_{\perp, \max} \simeq 0.08 B_p \left(\frac{R}{r_e}\right)^3 \theta_e = 0.08 B_e \theta_e \quad (13)$$

or

$$B_{\perp, \max} \simeq 1.2 \times 10^9 \text{G} B_{e,12} P^{-1/2} r_{e,6}^{1/2} \xi. \quad (14)$$

Here  $B_p$ ,  $B_e$ ,  $B_a$  are the magnetic fields at the surface, the emission point, and the absorption point, respectively,  $\theta_e = \xi \left(\frac{\Omega r_e}{c}\right)^{1/2}$  (according to the dipolar configuration),

and  $0 < \xi = \theta_s/\theta_{\text{pc}} < 1$  is the ratio of the field line magnetic colatitude at the surface,  $\theta_s$ , to the polar cap angle at surface,  $\theta_{\text{pc}} = \left(\frac{\Omega R}{c}\right)^{1/2}$ .

For  $l \ll r_a$  (this is the case for most of the generations except for the last one which will not pair produce again, see numerical results of HBG97, thus is a plausible approximation to describe the averaged cascade processes), we have  $r_a \simeq r_e$ ,  $B_a \simeq B_e$ , and equation (12) reads

$$B_\perp \simeq \frac{3}{4} B_e \frac{l}{r_e/\theta_e} = B_e \frac{l}{\rho_e}, \quad (15)$$

where

$$\rho_e \simeq \frac{4}{3} \frac{r_e}{\theta_e} = 9.2 \times 10^7 (\text{cm}) r_{e,6}^{1/2} P^{1/2} \xi^{-1} \quad (16)$$

is the curvature radius of field line at the emission point (assuming dipolar configuration). Equation (15) is identical with the approximation used in many previous analytic studies (e.g. RS75).

We now incorporate the correction of the field enhancement effect in curved spacetime. By taking into account the general relativistic effect, the magnetic field measured in a local rest frame of reference in curved spacetime reads (see Wasserman & Shapiro 1983 and GH94, but adopting magnetic moment  $B_p R^3/2$ , however.)

$$\begin{aligned} \mathbf{B}_{\text{curved}} &= B_{r, \text{curve}} \hat{r} + B_{\theta, \text{curve}} \hat{\theta} \\ &= -\frac{3B_p R^3 \cos \theta}{r_g^2 r} \left[ \frac{r}{r_g} \ln \left(1 - \frac{r_g}{r}\right) + 1 + \frac{1}{2} \frac{r_g}{r} \right] \hat{r} \\ &\quad + \frac{3B_p R^3 \sin \theta}{r_g^2 r} \left[ \left(\frac{r}{r_g} - 1\right) \ln \left(1 - \frac{r_g}{r}\right) + 1 - \frac{1}{2} \frac{r_g}{r} \right] \\ &\quad \times \left(1 - \frac{r_g}{r}\right)^{1/2} \hat{\theta}, \end{aligned} \quad (17)$$

where  $r_g = \frac{2GM}{c^2}$  is the Schwarzschild radius. Let us overlook the modification of the “dipole” configuration of this formula (the effect is actually almost canceled by the effect of the curved photon trajectory, GH94), and compare it with the magnetic field expression in the flat spacetime (note also adopting  $B_p R^3/2$  as the magnetic torque)

$$\begin{aligned} \mathbf{B}_{\text{flat}} &= B_{r, \text{flat}} \hat{r} + B_{\theta, \text{flat}} \hat{\theta} \\ &= \frac{B_p R^3 \cos \theta}{r^3} \hat{r} + \frac{B_p \sin \theta}{2r^3} \hat{\theta} \end{aligned} \quad (18)$$

We see the curved spacetime effect will increase the strength of the magnetic field by a factor of

$$q(r) = \frac{[B_{r, \text{curved}}^2(r) + B_{\theta, \text{curved}}^2(r)]^{1/2}}{[B_{r, \text{flat}}^2(r) + B_{\theta, \text{flat}}^2(r)]^{1/2}}. \quad (19)$$

With this correction, equations (10,12,13,14) should be modified by multiplying a factor of  $q(r)$ . Note that the factor  $q(r)$  is equivalent to the function  $f(\eta)$  introduced in HM98, which decreases with  $r$ , and converges to unity at infinity. For a typical neutron star with  $M = 1.4M_\odot$  and  $R = 10\text{km}$ , we have  $r_g/R \simeq 0.4$ , thus the modification factor at the surface is  $q(R) \sim 1.4$ , and  $q(r) \sim (1.18 - 1.25)$  for the height of 0.5-1 stellar radii, which is the interested region discussed in this paper (see details in Sect.2.5). Then the maximum perpendicular magnetic field (eq.[14]) now should be modified by multiplying a factor  $q(r_e)$ , which is

$$B_{\perp, \max, \text{curved}}(\text{nPSR}) \simeq 1.4 \times 10^9 \text{G} B_{e,12} P^{-1/2} r_{e,6}^{1/2} \xi \quad (20)$$

for normal pulsars, and

$$B_{\perp, \text{max, curved}}(\text{msPSR}) \simeq 5.1 \times 10^7 \text{G} B_{e,9} P_{-3}^{-1/2} r_{e,6}^{1/2} \xi \quad (21)$$

for millisecond pulsars. Here  $B_e = B_p \left(\frac{R}{r_e}\right)^3$  is still the field strength at the emission point in *flat* spacetime.

There is yet another effect, namely the “non-zero pitch angle” effect, that will reduce the attenuation length of the SR photons, which has been overlooked in some of the previous studies. The expressions of  $B_{\perp}$  (eqs.[10,12,15]) are derived assuming that photons are emitted along the tangent direction of the field line, which is not the case for higher generation SR photons which follow the direction of the pairs which have a non-zero pitch angle with respect to the field lines. Thus equations (10,12,15) have in fact underestimated the strength of the perpendicular field. However, the geometric relation in (10) could still be used by replacing the emission point  $(r_e, \theta_e)$  with the point  $(r_{e,0}, \theta_{e,0})$  where the  $\gamma$ -rays are emitted tangentially. Defining  $l_0$  as the distance between  $(r_{e,0}, \theta_{e,0})$  and  $(r_a, \theta_a)$ , and  $l$  as the mean free path of the SR  $\gamma$ -rays, i.e. the distance between  $(r_e, \theta_e)$  and  $(r_a, \theta_a)$  (see Fig.1 for illustration), again adopting  $\theta_e \ll 1$ , the perpendicular field is then

$$B_{\perp} = B_a \theta_e \frac{3r_e^2 l_0}{2r_a(r_e + l_0 - l)(2r_e + l_0 - l)}, \quad (22)$$

which is simply

$$B_{\perp} \simeq B_e \frac{l_0}{\rho_e} \quad (23)$$

when  $l < l_0 \ll r_e$ . This is just equation (15) by changing  $l$  to  $l_0$ . We see the higher the SR generation, the stronger the perpendicular fields, since  $l_0$  increases with generations. This effect will raise the value of  $\chi$  for pair-production with the same  $l_6$  (see Sect.2.2.3 and Fig.2) and hence, tend to increase the number of the SR generations. Such a “non-zero pitch angle” effect is non-relevant to the ICS branch, however, since the ICS photons are emitted by the pairs after emitting their perpendicular energies via SR, and hence, follow the tangential direction of the field line at the emission point.

### 2.2.3. How large is $\chi$ for pair production?

Equation (7) can give a self-consistent  $l_6$  and  $\chi$  for one-photon pair production. It is essential that the parameter  $\chi$  does not sensitively depend upon various parameters, since small changes in  $\chi$  correspond to exponentially large changes of  $l_6$ . Such a feature makes some simple analytic formulae available in analytic studies (e.g. RS75; LWS94; WSL97). In these models,  $\chi$  is adopted as 1/15. However, in order to treat the process more precisely, it is still worth examining the possible variation of  $\chi$  for different pulsar parameters. A smaller  $l_6$  can increase  $\chi$  and hence increase the total number of generations (i.e. the generation order parameter, LWS94, WSL97, also see Sect.2.3 and 2.4). In fact, Zhang et al. (1997b) has adopted  $\chi = 0.09, 0.12$  to estimate the parameters of different polar gap modes.

Using (7), (16) and (15), one can get a more accurate value of  $\chi$  when  $B_e$ ,  $P$ ,  $r_{e,6}$  (these three parameters are specified for a certain pulsar and an acceleration model),

$l_6$  (this parameter depends on the  $\gamma$ -ray energy) and  $\xi$  (depends on the field line) are given

$$\chi = \frac{4}{3} \ln^{-1} [0.01 B_e P^{-1/2} l_6^2 r_{e,6}^{-1/2} \xi] \quad (24)$$

Figure 2 plots the dependence of  $1/\chi$  on  $l_6$  (corresponding to different  $E_{\gamma}$ ) for two sets of parameters: one set is for a typical normal pulsar with  $B_e = 10^{12} \text{G}$ ,  $P = 0.1 \text{s}$ ,  $r_{e,6} = 1.8$  and  $\xi = 1$ ; another is for a typical millisecond pulsar with  $B_e = 5 \times 10^8 \text{G}$ ,  $P = 0.005 \text{s}$ ,  $r_{e,6} = 1.2$  and  $\xi = 1$ . Note that different adoptions of  $r_{e,6}$  are based on the HM98 model (see Sect.2.5). We found that, the parameter  $\chi$  has deviated from 1/15 for most of the cases. For most of the generations, we have  $l_6 \ll 1$  (see numerical results in HBG97), thus  $\chi$  is larger than 1/15. For millisecond pulsars, the values of  $\chi$  are even larger.

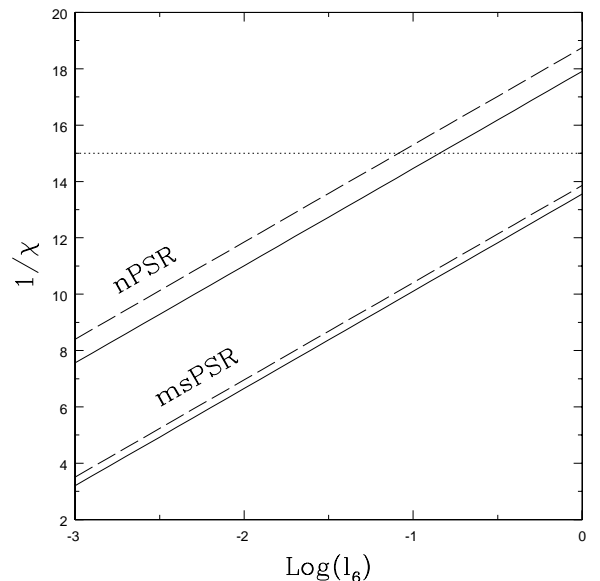


FIG. 2.— The  $l_6$  dependence of the critical value of  $\chi$  for  $\gamma - B$  pair production ( $1/\chi$  is plotted). The upper two lines are for a typical normal pulsar with  $P = 0.1 \text{s}$ ,  $B_{e,12} = 1.0$ ,  $r_{e,6} = 1.8$  (thus  $B_{p,12} = 5.8$ ), and  $\xi = 1$ ; the lower two lines are for a typical millisecond pulsar with  $P = 0.005 \text{s}$ ,  $B_{e,12} = 5.0 \times 10^{-4}$ ,  $r_{e,6} = 1.2$  and  $\xi = 1$  (thus  $\log B_p = 8.9$ ). The dashed lines are for the case of ‘tangentially’ emitting, and the solid lines are for the case with an estimate correction of the non-zero pitch angle effect. The dotted line marks the conventional value  $\chi = 1/15$ .

The critical  $\chi$  for pair production could be further enhanced by including “non-zero pitch angle” effect as discussed above. With (23) rather than (15), the equation (24) now becomes

$$\chi = \frac{4}{3} \ln^{-1} [0.01 B_e P^{-1/2} l_6 l_{0,6} r_{e,6}^{-1/2} \xi] \quad (25)$$

At higher generations,  $l_{0,6}$  is larger than  $l_6$ . We have adopted  $l_{0,6} = 3l_6$  for normal pulsars and  $l_{0,6} = 1.5l_6$  for millisecond pulsars to cover this effect. The different adoptions reflect different generation numbers in normal and millisecond pulsars. The results are also shown in Fig.2.

With the results in Fig.2, we come to some “recommended” values for the critical  $\chi$ . When calculating photon escaping energy (see Sect.2.2.4), it is appropriate to

adopt a smaller  $\chi$  since  $l_6$  of the last generation  $\gamma$ -rays is usually around unity (recall  $B_{\max}$  is achieved when  $l \simeq r_e/3$ , also see numerical results of HBG97). However, when describing the cascade process, a larger  $\chi$  should be adopted, since the averaged  $l_6$  is much less than unity. In our following analytic formulae, we'll adopt

$$\chi_{\text{esc}}(\text{nPSR}) \sim 1/16, \quad \chi_{\text{cas}}(\text{nPSR}) \sim 1/12 \quad (26)$$

for normal pulsars, and

$$\chi_{\text{esc}}(\text{msPSR}) \sim 1/12, \quad \chi_{\text{cas}}(\text{msPSR}) \sim 1/8 \quad (27)$$

for millisecond pulsars, according to the results of Fig.2.

#### 2.2.4. Photon escaping energy

Photon escaping energy is the energy below which the magnetosphere is transparent. A numerical result of the escaping energy of photons is shown in Fig.2 of HBG97. With (8), adopting  $B_{\perp}$  as the  $B_{\perp, \max}$  described in (20) and (21) in which the correction of curved spacetime effect has been included, also choosing the recommended  $\chi_{\text{esc}}$  in equations (26,27), we get

$$E_{\gamma, \text{esc}}(\text{nPSR}) \simeq 2.0 \text{GeV} B_{e,12}^{-1} P^{1/2} r_{e,6}^{-1/2} \xi^{-1} \chi_{1/16} \quad (28)$$

for normal pulsars and

$$E_{\gamma, \text{esc}}(\text{msPSR}) \simeq 73 \text{GeV} B_{e,9}^{-1} P_{-3}^{1/2} r_{e,6}^{-1/2} \xi^{-1} \chi_{1/12} \quad (29)$$

for millisecond pulsars. Note these relations are quite different from equation (36) of Hardee (1977), who has adopted the incorrect form of  $\gamma$ -ray absorption formula. As pointed out by Zheng, Zhang & Qiao (1998), although the general formula of  $\gamma$ -ray attenuation including both the perpendicular magnetic fields and the electric fields derived by Daugherty & Lerche (1975) is correct, when applying it to the situation of pulsars, the contribution of the induced electric fields are actually of no importance, since in the static frame (rather than the co-rotating frame), the emission direction is not strictly along the direction of the field line due to Lorentz transformation. Hardee (1977) has used the Daugherty & Lerche's formula by assuming that the photons are emitted tangentially along the field line in the static frame, and thus gave a incorrect larger absorption coefficient<sup>3</sup>. WSL97 obtained a similar equation (their eq.[10]) as our (28), but they did not include the general relativistic correction and the non-zero pitch angle effect.

#### 2.3. Recursion relations between different generations

There exist some simple recursion relations between the characteristic emission frequency of both the two-branch filial-generation (SR and ICS) photons and the parent-generation photons. Consider a certain parent generation  $\gamma$ -ray with dimensionless energy  $\epsilon_i$  (the origin of this photon is not important), for SR branch, the typical energy of the filial-generation  $\gamma$ -rays is

$$\epsilon_{i+1, \text{SR}} = \frac{3}{2} \gamma_{i+1}^2 B'_e \sin \theta_{\text{kB}} = \frac{3}{4} \chi \epsilon_i \quad (30)$$

where  $\gamma_{i+1} = \epsilon_i/2$  is the Lorentz factor of the filial-generation pairs following the direction of the parent photon, which impacts the field with an angle of  $\theta_{\text{kB}}$ . Define  $\kappa = \epsilon_{i+1}/\epsilon_i$  as the energy reduction factor of the adjacent generations, we have (LWS94; WSL97)

$$\kappa_{\text{SR}} = \frac{\epsilon_{i+1, \text{SR}}}{\epsilon_i} = \frac{3}{4} \chi. \quad (31)$$

Recalling the recommended  $\chi_{\text{cas}}$  values in equations (26,27), we have

$$\kappa_{\text{SR}}(\text{nPSR}) \sim 1/16 \quad (32)$$

for normal pulsars and

$$\kappa_{\text{SR}}(\text{msPSR}) \sim 1/11 \quad (33)$$

for millisecond pulsars. Note in (30) we have adopted the classical formula to describe the SR process. In the strong magnetic fields, however, the SR process should be strictly described quantum-mechanically as the transitions between Landau levels with adjacent energy interval of  $\Delta E_L \simeq \hbar \omega_B = 11.2 B_{e,12} \text{keV}$  (for a review, see Harding 1991). The comparisons of the quantum and classical treatments of the SR process have been presented in Harding & Preece (1987) and Baring (1988). The classical description is not a bad approximation as long as the Landau state number of the pairs is large (e.g.  $> 20$ ), which means that critical SR photon energy is much larger than  $\Delta E_L$ , and the field strength is not too high, i.e.,  $B' \leq 0.1$  (see numerical results in Harding & Preece 1987, note this is the same condition for the asymptotic formula (7) to hold). Both conditions are fulfilled in most cases discussed in this paper (see Sect.2.5).

For the ICS branch filial-generation, the typical energy of the emitting (scattering) photon ( $(i+1)$ -th generation) is determined by the Lorentz factor of the pairs ( $(i+1)$ -th generation) after they have emitted their perpendicular energy via SR. Suppose such Lorentz factor is  $\gamma_{i+1, \parallel}$ , the typical ICS photon energy is simply (e.g. Zhang et al. 1997a)

$$\epsilon_{i+1, \text{ICS}} = 2\gamma_{i+1, \parallel} B'_e \quad (34)$$

for resonant scatterings. Note essentially, this typical energy depends on the local field strength, but does not depend on the incident angle of the scatterings. This feature can be understood as follows: a soft photon with frequency  $\epsilon_0$  which impacts by an incident angle of  $\theta = \cos^{-1} \mu$  with an electron with energy  $\gamma_{\parallel}$ , will be inverse Compton scattered to a maximum frequency of  $\epsilon_s = 2\gamma_{\parallel}^2 (1 - \beta_{\parallel} \mu) \epsilon_0$ . For a resonant scattering occurring, the incident energy  $\epsilon_0$  should be Lorentz-boosted to exactly the cyclotron energy  $\epsilon_B = B'$  in the electron rest frame, i.e.,  $\epsilon_0 = B'/[\gamma_{\parallel} (1 - \beta_{\parallel} \mu)]$ . Thus the angular factors in both expressions are exactly canceled in the final result. In other words, the electron can "pick up" the right energies of the photons from different directions and resonant scatter them to contribute to the same characteristic energy (34).

<sup>3</sup>Note that in Zheng, Zhang & Qiao (1998), there are some mis-comments on the work of Harding, Tademaru, & Esposito (1978), Harding (1981), and Daugherty & Harding (1982), who have correctly treated the absorption problem by including the "aberration of the emission directions" in the static frame.

Another point is that in (34), we have again overlooked the possible variation of  $B_e$  for different generations. (We did not specify  $B_{e,i}$  for a certain generation  $i$ .) We will adopt this assumption throughout the paper, since it is sound only except for the very last generation or when resonant scattering condition (4) fails so that the ICS mean free path (5) becomes long. Even so, the correction to our results is still tiny.

The parallel Lorentz factor of the  $(i+1)$ -th generation pairs is (see Appendix A, also WSL97)

$$\gamma_{i+1,\parallel} = \frac{\gamma_{i+1}}{[1 + (\gamma_{i+1}^2 - 1) \sin^2 \theta_{\text{kB}}]^{1/2}}. \quad (35)$$

Noting that  $\gamma_{i+1} = \epsilon_i/2$  (each of the  $(i+1)$ -th pair gain one half of the  $i$ -th generation photon energy), as long as  $\gamma_{i+1} \gg 1$  (this is the case for most generations), we have  $(\gamma_{i+1}^2 - 1) \sin^2 \theta_{\text{kB}} \simeq (\epsilon_i/2 \sin \theta_{\text{kB}})^2 = (\chi/B'_e)^2$ , which only depends on  $B_e$  when we adopt a constant  $\chi$ . Define

$$\eta_{\parallel} = \frac{\gamma_{i,\parallel}}{\gamma_i} \quad (36)$$

as the portion of the particle energy which goes to the ICS branch, from (35) we obtain

$$\eta_{\parallel} \simeq \frac{1}{[(\chi/B'_e)^2 + 1]^{1/2}}. \quad (37)$$

This is independent on the generation order  $i$  if we neglect the very small variation of  $B_e$  in different generations. Note this is an essential point, since the energy distribution between the two-branch (SR and ICS) filial generations is settled for a given pulsar in different generations of the cascades. Using (26,27), we get

$$\eta_{\parallel}(\text{nPSR}) \simeq \frac{1}{(13.5B_{e,12}^{-2} + 1)^{1/2}} \quad (38)$$

for normal pulsars, and

$$\eta_{\parallel}(\text{msPSR}) \simeq 1.8 \times 10^{-4} B_{e,9} \quad (39)$$

for millisecond pulsars. We see only a small portion of energy is left in the ICS branch for millisecond pulsars, since  $B_e$  is much lower. This is the third factor to reduce the importance of the ICS-branches for the millisecond pulsars. Recall the other two factors are: longer mean free path (eq.[5]) and possible failure of the second resonant condition (eq.[6]). These are the reasons why the non-thermal X-rays are usually not important compared with the thermal emission for millisecond pulsars, as will be shown in Sect.3.3.

We can also define the energy portion going to the SR branch. This is just

$$\eta_{\perp} = 1 - \eta_{\parallel}, \quad (40)$$

and was denoted as ‘‘energy conversion efficiency’’ in WSL97. Similarly, we can derive different  $\eta_{\perp}(\text{nPSR})$  and  $\eta_{\perp}(\text{msPSR})$  using (38) and (39), respectively.

With (34), noting  $\gamma_{i+1,\parallel} = \eta_{\parallel} \gamma_{i+1}$ , and again  $\gamma_{i+1} = \epsilon_i/2$ , we have

$$\kappa_{\text{ICS}} = \frac{\epsilon_{i+1,\text{ICS}}}{\epsilon_i} = \eta_{\parallel} B'_e, \quad (41)$$

or

$$\kappa_{\text{ICS}}(\text{nPSR}) = \frac{0.0227 B_{e,12}}{(13.5 B_{e,12}^{-2} + 1)^{1/2}} \simeq \frac{1}{160} B_{e,12}^2 \quad (42)$$

for normal pulsars (assuming  $B_{e,12} \leq 1$ ) and

$$\kappa_{\text{ICS}}(\text{msPSR}) \simeq 4.1 \times 10^{-9} B_{e,9}^2 \quad (43)$$

for millisecond pulsars. This means that, except for pulsars with high magnetic fields, ICS branches usually have a more significant decrease of the typical photon energy than SR branches, especially for millisecond pulsars.

#### 2.4. Generation order parameters

The so-called ‘‘generation order parameter’’ was first introduced by Lu, Wei & Song (LWS94) and improved by Wei, Song & Lu (WSL97). In their work, the authors introduced the non-integer generation order parameter  $\zeta$  to describe the conventional curvature-synchrotron cascades based on the RS75 acceleration model, and showed that the observed  $\gamma$ -ray pulsars tend to have relative large  $\zeta$ s. Such a concept can delineate the sketch of the cascade process, and, to some extent, compensate the shortcoming of the analytic ‘‘recursion’’ descriptions, i.e., the ignorance of the detailed spectral features of different generations.

In our full-cascade picture, the complicated two-branch filial-generation feature makes it impossible to describe the whole process with one single generation order parameter. But we can still borrow their definitions in our studies.

Suppose the primary generation  $\gamma$ -rays have a typical energy  $E_0$  (this is model-dependent, we’ll give the expressions in the HM98 model (eqs.[48,51]) in Sect.2.5), there will be altogether

$$\zeta_{\text{SR}} = \frac{\log(E_{\text{esc}}/E_0)}{\log(\kappa_{\text{SR}})} + 1 \quad (44)$$

SR generations before the photon energies are reduced to  $E_{\text{esc}}$ . Note the term  $(+1)$  in (44) is to ensure  $\zeta = 1$  for the primary  $\gamma$ -rays (with energy  $E_0$ ).  $\zeta_{\text{SR}}$  is just the generation order parameter defined by LWS94 and WSL97. In our full cascade scenario, this parameter only describe the typical cascade branches with pure SR generations. Similarly, we can define another parameter

$$\zeta_{\text{ICS}} = \frac{\log(E_{\text{esc}}/E_0)}{\log(\kappa_{\text{ICS}})} + 1 \quad (45)$$

to describe the pure ICS cascade branches. However, neither (44) nor (45) can describe the ‘‘crossed’’ generations (e.g. ICS branch from the SR parent generation or vice versa). We will define some more general generation order parameters (e.g. [78],[85]) to construct an analytic estimate formula of pulsar X-ray luminosities (see eqs.[77,84]). For most pulsars, the ICS branch photons usually do not pair-produce any more (see Sect.2.5, also SDM95). This can further simplify the description (see details in Sect.3.3).



### 2.5. HM98 acceleration model

Here before, we have not specified an acceleration model. The descriptions above are valid for any polar cap acceleration model once  $E_0$  is specified. There are generally two subclasses of polar cap acceleration models. One subclass is the vacuum gap model first proposed by RS75, and modified by Usov & Melrose (1995; 1996) and Zhang et al. (Zhang & Qiao 1996; Zhang et al. 1997a,b). Another subtype model is the space-charge-limited flow model (Arons & Scharlemann 1979; Arons 1983), which assumes free flow of particles from the surface. Such a model is improved by Muslimov & Tsygan (1992) and Muslimov & Harding (1997) by incorporating the frame dragging parallel electric fields, and finally HM98 imposed the zero  $E_{\parallel}$  boundary condition at the pair formation front (PFF) to treat the accelerator more realistically. In reality, the environment of different pulsars could vary much from one to another, so that the above-mentioned two different types of inner accelerators may anchor in different pulsars. For example, there is growing evidence showing that a handful of the “drifting” radio pulsars seem to have the RS-type vacuum accelerators in their polar cap region (Deshpande & Rankin 1999; Vivekanand & Joshi 1999). However, theoretical arguments, i.e., the so-called binding energy problem encountered by the RS75 model (Jones 1985, 1986; Neuhauser et al. 1986, 1987), support the space-charge-limited flow acceleration scheme. In this paper, we will adopt the HM98 acceleration model uniformly for all the pulsars.

No simple analytic description for all pulsars is available in the HM98 model due both to the complicated form of  $E_{\parallel}$  within the gap and to the screening details. Nevertheless, a general accelerating picture is available, i.e.,  $E_{\parallel}$  grows approximately linearly if the gap length  $S_c$  is smaller than the “effective” polar cap radius  $r_{pc,E}$  (assuming an effective star surface  $R_E \sim (1.5 - 2)R$ ), or will be saturated to an almost constant value above  $r_{pc,E}$  if  $S_c > r_{pc,E}$ . Hereafter we will define the cases with or without field saturation as the regime I and II, respectively. In principle, both CR and ICS of the primary particles should be taken into account. However, for most pulsars (except for high  $B$  pulsars), as pointed out by HM98, as long as ICS dominates in the accelerator, the accelerator itself is unstable, since the upward ICS occurs in the resonant regime, while the downward ICS occurs in the Klein-Nishina regime. Thus the final stable accelerator should be controlled by CR. In fact, the “effective surface”  $R_E$  is determined by the criterion that beyond this height, the ICS energy loss rate is less than the CR energy loss rate (see HM98). In regime I, the CR-controlled gap length ( $S_c$ ), the maximum typical Lorentz factor of the primary particles ( $\gamma_0$ ), as well as the characteristic CR photon energy emitted by the primary particles, i.e.,  $E_0 = \frac{3}{2} \frac{\hbar c}{\rho_e}$ , could be approximately obtained using (A3) of HM98, which read (see also eqs.[77,79] in HM98, in which there are some minor computing errors)

$$S_c(\text{I}) \simeq 4.2 \times 10^4 \text{cm} B_{p,12}^{-4/7} P^{4/7} R_{E,6}^{16/7} (\cos \alpha)^{-3/7}, \quad (46)$$

$$\gamma_0(\text{I}) \simeq 8.2 \times 10^7 B_{p,12}^{-1/7} P^{1/7} R_{E,6}^{4/7} (\cos \alpha)^{1/7}, \quad (47)$$

and

$$E_0(\text{I}) \simeq 178(\text{GeV}) B_{p,12}^{-3/7} P^{-1/14} R_{E,6}^{17/14} (\cos \alpha)^{3/7}, \quad (48)$$

respectively, where  $\alpha$  is the inclination angle of the neutron star. For the regime II, we adopt the saturated  $E_{\parallel}$  presented in (A5) of HM98, and obtain the different expressions which read

$$S_c(\text{II}) \simeq 3.2 \times 10^6 \text{cm} B_{p,12}^{-1} P^{7/4} R_{E,6}^{-2} (\cos \alpha)^{-3/4}, \quad (49)$$

$$\gamma_0(\text{II}) \simeq 1.4 \times 10^7 P^{-1/4} R_{E,6}^2 (\cos \alpha)^{1/4}, \quad (50)$$

and

$$E_0(\text{II}) \simeq 0.88(\text{GeV}) P^{-5/4} R_{E,6}^{11/2} (\cos \alpha)^{3/4}. \quad (51)$$

The emission height discussed in the previous sections is then

$$r_{e,6} = R_{E,6} + S_{c,6}. \quad (52)$$

It is worth noting that, the primary particles actually lose their energies within and above the accelerator via both CR and ICS, and the ICS process has a different typical  $E_0$ , so that it will also contribute to a component in the final  $\gamma$ -ray spectrum and change the generation structure to some extent. But such modifications are not prominent. Furthermore, the energetics of both the CR and ICS photons are from the kinetic energy of the primary particles (47,50), thus the variation of the detailed primary photon spectrum does not change much the luminosity predictions presented in Sect.3, where we adopt the primary luminosity as the total polar cap particle luminosity (see [54]).

Since regime I is limited by regime II, in principle, we should adopt the minimum of  $\gamma_0(\text{I})$  and  $\gamma_0(\text{II})$  as the real  $\gamma_0$  (and hence  $E_0$ ) for a certain pulsar. The critical condition to separate the two regimes could be obtained by equating eq.(47) with (50). Thus a pulsar should be in regime I if

$$B_{p,12}^{1/7} P^{-11/28} R_{E,6}^{10/7} (\cos \alpha)^{3/28} > 6.0, \quad (53)$$

and in regime II otherwise. Note that this is just a rough analytic treatment. Numerically, there should be no such distinct boundary, and the two regimes should meet smoothly.

With (48) or (51), one can get explicit expressions of the generation parameters from (44) and (45). This completes the analytic description of the full cascade process. It is worth noting that  $1 < \zeta_{\text{ICS}} < 2$  for most pulsars (see Table 2). Such an issue was also noted by SDM95, who thus suggested that ICS branches will not further produce filial-generation pairs. However, for the high field pulsars, this is not necessarily the case (also see Table 2). In our analytic formula below, without losing generality, we will also cover the possible contributions from the ICS-photon-produced pairs (see eq.[77]).

HM98 has discussed the positron backflow feedback quantitatively. Though the complication of the  $E_{\parallel}$  screening process prevents an accurate determination of the fraction of backflowing positrons, an upper limit of such a flow is readily available from the model, which is useful to estimate the maximum thermal X-ray luminosities due to polar cap heating. The expressions of such maximum thermal X-ray luminosities are shown in equations (69) and (72) (see Sect.3.2).

## 3. LUMINOSITY PREDICTIONS

## 3.1. Gamma-ray luminosity

Harding (1981) pointed out that by assuming a roughly constant potential in the inner accelerators for different pulsars (so that the primary particles gain almost the same energy  $\gamma_0$  for different pulsars), the total polar cap “luminosity”

$$L_{\text{pc}} = \gamma_0 m c^2 \dot{N}_p \quad (54)$$

is then proportional to  $B_p/P^2$ , since the particle flow rate

$$\dot{N}_p = c n_{\text{GJ}} \pi r_p^2 = 1.4 \times 10^{30} R_6^3 B_{p,12} P^{-2} (\cos \alpha) \quad (55)$$

itself is proportional to  $B_p/P^2$ , where  $n_{\text{GJ}} \simeq \frac{\Omega \cdot \mathbf{B}}{2\pi e c}$  is the Goldreich-Julian (1969) number density. This will give a natural interpretation of the observed relationship of  $L_\gamma \propto (L_{\text{sd}})^{1/2}$  if the polar cap “luminosity” is completely converted to  $\gamma$ -ray emission. However, in the canonical CR-SR (DH96) or ICS-SR (SDM95) cascade picture, the expected  $\gamma$ -ray luminosity  $L_\gamma$  is not fully identical to  $L_{\text{pc}}$ , since only the perpendicular portion of the energies of the pairs goes to the next generation radiation. More specifically, one has (WSL97)

$$L_\gamma(\text{canonical}) \simeq L_{\text{pc}} \eta_\perp^{\zeta_{\text{SR}}}, \quad (56)$$

which will deviate from  $L_{\text{pc}}$  to some extent. The deviation is more significant for the pulsars with small  $\eta_\perp$  and large  $\zeta_{\text{SR}}$  (e.g. PSR 1509-58, see Fig.3, Table 1). In the full two-branch cascade picture described above, it is safe to regard

$$L_\gamma(\text{full}) \simeq L_{\text{pc}}, \quad (57)$$

since the ICS branches “pick up” the “lost” parallel kinetic energies of the particles also to radiation, so that almost 100% of the polar cap “luminosity” is converted to high energy radiation. Although not all these energies are converted to  $\gamma$ -rays (in fact, the non-thermal X-ray emission is also part of this energy budget, see Sect.3.3 below), the majority of this energy output is in the  $\gamma$ -ray band.

In the HM98 model, the typical energy of the primary particles  $\gamma_0$  turns out to be very weakly dependent on the pulsar parameters (eqs.[47,50]), especially for the young pulsars in regime I (only Geminga and PSR 1055-52 are in regime II). This is in agreement with the assumption of Harding (1981). With eqs.(57,54,55) and (47) or (50), and

$$L_{\text{sd}} = -I\Omega\dot{\Omega} \simeq 9.68 \times 10^{30} B_{p,12}^2 P^{-4} I_{45} \quad (58)$$

( $I = 10^{45} I_{45}$  is the moment of inertia), the  $\gamma$ -ray luminosity is finally

$$\begin{aligned} L_\gamma(\text{full, I}) &\simeq 9.4 \times 10^{31} \text{erg} \cdot \text{s}^{-1} B_{p,12}^{6/7} P^{-13/7} R_{E,6}^{4/7} (\cos \alpha)^{8/7} \\ &= 3.0 \times 10^{16} B_{p,12}^{-1/7} P^{1/7} R_{E,6}^{4/7} (\cos \alpha)^{8/7} (L_{\text{sd}})^{1/2}, \end{aligned} \quad (59)$$

for regime I, and

$$\begin{aligned} L_\gamma(\text{full, II}) &\simeq 1.6 \times 10^{31} \text{erg} \cdot \text{s}^{-1} B_{p,12} P^{-9/4} R_{E,6}^2 (\cos \alpha)^{5/4} \\ &= 0.5 \times 10^{16} P^{-1/4} R_{E,6}^2 (\cos \alpha)^{5/4} (L_{\text{sd}})^{1/2}, \end{aligned} \quad (60)$$

for regime II. This almost reproduces the  $L_\gamma \propto (L_{\text{sd}})^{1/2}$  feature (also see Fig.3).

A natural implication of the  $L_{\text{pc}} \propto (L_{\text{sd}})^{1/2}$  dependence is that the  $\gamma$ -ray emission efficiency,  $L_{\text{pc}}/L_{\text{sd}}$ , will increase for the pulsars with lower  $L_{\text{sd}}$ . Physically, such an efficiency can not be greater than unity. Since as  $L_{\text{pc}}$  approaches  $L_{\text{sd}}$  the accelerator should be in regime II (saturated), we can use (60) and (58) to get the constraint

$$B_{p,12} P^{-7/4} R_{E,6}^{-2} (\cos \alpha)^{-5/4} \geq 1.65. \quad (61)$$

Such a line is also close to the pulsar pair formation “deathline” (for a detailed discussion of the deathlines, see Zhang, Harding & Muslimov (1999)). The luminosity formulae (59,60) are no longer valid when (61) fails. None of the observed spin-powered X-ray pulsars studied in this paper are beyond this line.

In Table 1 and Fig.3, we compare the broad-band high energy luminosities of the 8  $\gamma$ -ray pulsars with the theoretical predictions both in the full cascade model and the canonical CR-SR cascade model. Though the  $L_\gamma \propto (L_{\text{sd}})^{1/2}$  feature is reported using  $\gamma$ -ray luminosities above 100KeV (Thompson et al. 1997), here we adopt the latest luminosity data above 1eV for the 7 previously known  $\gamma$ -ray pulsars including the new data of PSR 1055-52 (Thompson et al. 1999), which also clearly shows the same trend, and indicates that most emission is spread in the  $\gamma$ -ray band. For the newly discovered  $\gamma$ -ray pulsar PSR 1046-58, we adopt the luminosity data above 400MeV (Kaspi et al. 1999). As shown in Fig.3, all these data just meet our model prediction  $L_\gamma(\text{full})$  (eqs.[59,60]) well, which is essentially the polar cap luminosity  $L_{\text{pc}}$  (eq.[54]). The model parameters we adopt are:  $\alpha = 30^\circ$  and  $R_{E,6} = 1.8$ . It is clear that the full cascade model shows a much better fit to the observations than the canonical model which predicts lower  $\gamma$ -ray luminosities (eq.[56]) (see Fig.3), especially for PSR 1509-58. The small differences between the full-cascade predictions and the observations are within the range of different  $\alpha$  and slightly different  $R_{E,6}$ . Thus our model is in good agreement with the observations. Note that the present description is incomplete for the high  $B$  pulsar PSR 1509-58 (with  $\log B_p = 13.49$ ). In such strong fields, the resonant frequency is much higher, and the downward ICS of the positrons also occurs in the resonant regime (HM98). The anisotropy of ICS processes then disappears and the accelerator should still be located at the neutron star surface, with ICS as the controlled mechanism. However, photon splitting will also play an important role in high  $B$  pulsars (HBG97), so that the cascade is more complicated and includes both pair production and photon splitting. All these effects may alter the luminosity predictions of high  $B$  pulsars significantly, both for  $\gamma$ -rays and also for X-rays as well.

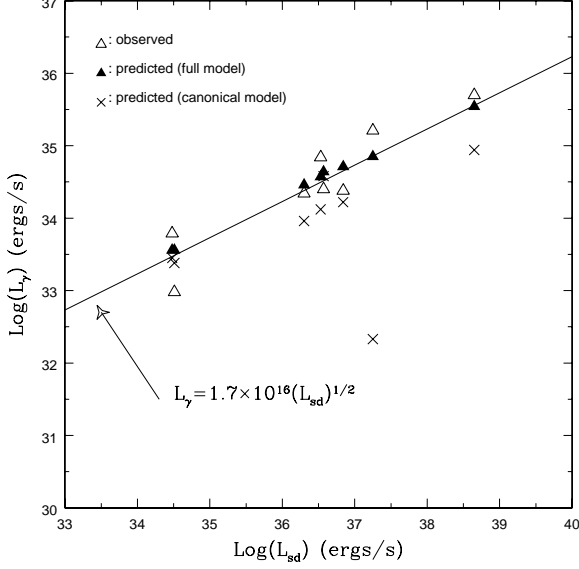


FIG. 3.— Comparison of the observed broad-band luminosities for the 7  $\gamma$ -ray pulsars and  $\gamma$ -ray luminosity of PSR 1046-58 above 400MeV with the model predictions in both the full cascade and the canonical CR(ICS)-SR cascade models. Note how the full cascade model ‘picks up’ the luminosities which the canonical model has ‘lost’, and clearly reproduces the  $L_\gamma \propto (L_{sd})^{1/2}$  feature.

It is also of interest to examine  $\gamma$ -ray luminosities of the millisecond pulsars. According to (60), usually the millisecond pulsars also have considerable  $\gamma$ -ray luminosities ( $\propto (L_{sd})^{1/2}$ ). However, due to their weak field strengths, the escaping photon energy is quite high (eq.[29]). As a result,  $\gamma$ -ray spectra of the millisecond pulsars are expected to be very hard, with the lowest characteristic SR energy (eq.[74]) about 150GeV, and the detectable photon number is fewer. Future missions, such as GLAST, may detect emission from these sources.

### 3.2. Thermal X-ray luminosity

As reviewed in Sect.2.1, there are many possible mechanisms to account for both the full surface and the hot polar cap thermal emission components from neutron stars. Here we will treat the full surface emission by adopting a simple “standard” cooling model, and treat the hot spot emission using the polar cap heating scenario predicted by the HM98 model.

#### 3.2.1. Full surface thermal emission: neutron star cooling

Neutron star cooling is the results of many different mechanisms, the physical details of some of which are still poorly known. Thus there are many uncertainties in different models (see Shapiro & Teukolsky (1983) for a review). In our calculation, we use a rough relation

$$\begin{aligned} \log T_{s,6} &= -0.1 \log \tau + 0.37 & \log \tau \leq 5.2 \\ \log T_{s,6} &= -0.5 \log \tau + 2.45 & \log \tau > 5.2 \end{aligned}, \quad (62)$$

which is obtained by a rough fit to the latest detailed numerical model of Schaab et al. (1999, their Fig.3), and is consistent with the standard “modified URCA” neutrino

<sup>4</sup>Note that this estimate of  $L_{e^+, \max}$  is much smaller than that given in eqs.(55,59) of HM98 because the screened accelerator length has been included here.

cooling plus photon cooling model reviewed in Shapiro & Teukolsky (1983). Here,  $\tau = P/2\dot{P}$  is the spin-down age of the pulsars. The reasons for us to adopt such a simple treatment are as follows: Firstly, such simple cooling models are not inconsistent with the observations (BT97; Schaab et al. 1999). Secondly, as long as the resonant ICS condition (4) is satisfied, our non-thermal luminosity predictions are insensitive to the temperature of the soft photons. Thus some extent of inaccuracy in the full-surface temperature adoption has little influence on the final results. Thirdly, in the polar cap cascade scenarios, it is unlikely to form a nearly static pair “blanket” near the surface, as assumed in the outer gap models. Hence, there should be no “reflected” full-surface thermal emission component. Furthermore, the outer gap models did not compare their soft thermal emission prediction with the observations, so that the assumption can not be justified.

#### 3.2.2. Polar cap heating

As discussed in Sect.2.5, the complication of the  $E_{\parallel}$  screening process makes it difficult to treat the positron backflow accurately, so that an explicit analytic description of the polar cap heating is not available. In principle, the maximum backflow positron rate  $\dot{N}_{e^+, \max}$  could be estimated by multiplying the polar cap current  $\dot{N}_p$  (eq.[55]) with a factor

$$f \simeq \left| \frac{(\nabla \cdot \mathbf{E})_{\parallel} / (4\pi)}{2\rho_{GJ}} \right|, \quad (63)$$

so that<sup>4</sup>

$$L_{e^+, \max} = \gamma_0 m c^2 \dot{N}_{e^+, \max} = f L_{pc}, \quad (64)$$

since  $E_{\parallel}$  determines the charge density required for screening, and the factor (1/2) accounts for the readjustment of the primary current due to the backflow current. However, due to the mathematical complications of the space-charge-limited flow model with frame-dragging included (Muslimov & Tsygan 1992; Muslimov & Harding 1997; HM98), a simple general expression is not available. For the unsaturated case, the gap is pancake-shaped, and the boundary conditions at the open field lines are not important. Thus one has  $(\nabla \cdot \mathbf{E})_{\parallel} / (4\pi) \simeq (\nabla \cdot \mathbf{E}) / (4\pi)$ , which is essentially  $(\rho - \rho_{GJ})$ , so that

$$\begin{aligned} f(I) &\simeq \left| \frac{\rho - \rho_{GJ}}{2\rho_{GJ}} \right| \simeq \frac{\eta_*^2 \kappa (1 - \eta^{-3})}{(1 - \eta_*^2 \kappa \eta^{-3})} \\ &= \frac{0.075 (R_{E,6}^{-3} - r_{e,6}^{-3})}{1 - 0.15 r_{e,6}^{-3}}, \end{aligned} \quad (65)$$

where eqs.(10,11) of HM98 has been used, ( $\sin \alpha$ ) term is neglected, and  $\eta_* = R/R_E = R_{E,6}^{-1}$ ,  $\eta = r/R_E$ ,  $\kappa = (r_g/R_E)(I/MR^2) = \kappa_0 R_{E,6}^{-1}$ ,  $\kappa_0 = (r_g/R)(I/MR^2) \sim 0.15$  have been adopted. Since usually  $S_c(I) \ll R$ , with (52), one can further derive

$$f(I) \simeq 0.23 R_{E,6}^{-3} z, \quad (66)$$

where

$$z = S_c(I)/R_E = 4.2 \times 10^{-2} B_{p,12}^{-4/7} P^{4/7} R_{E,6}^{9/7} (\cos \alpha)^{-3/7}, \quad (67)$$

and eq.(46) has been used. If this backflow energy is entirely converted to thermal emission at the hot polar cap, then the maximum polar cap thermal X-ray luminosity should be

$$L_{x,pc,max} \simeq L_{e^+,max}, \quad (68)$$

which is

$$L_{x,pc,max}(I) \simeq 9.1 \times 10^{29} \text{erg} \cdot \text{s}^{-1} B_{p,12}^{2/7} P^{-9/7} R_{E,6}^{-8/7} (\cos \alpha)^{5/7}, \quad (69)$$

for regime I. The maximum polar cap temperature (assuming an area of  $\pi r_{pc}^2$ , where  $r_{pc} = \theta_{pc} R = 1.45 \times 10^4 P^{-1/2} \text{cm}$ ) is hence

$$T_{pc,max}(I) = \left( \frac{L_{x,th,max}(I)}{\sigma \pi r_{pc}^2} \right)^{1/4} \\ \simeq 2.2 \times 10^6 \text{K} B_{p,12}^{1/14} P^{-1/14} r_{e,6}^{-2/7} (\cos \alpha)^{5/28}, \quad (70)$$

where  $\sigma = 5.67 \times 10^{-5} \text{ergs} \cdot \text{cm}^{-2} \cdot \text{K}^{-4} \cdot \text{s}^{-1}$  is Stefan's constant.

For regime II (saturated case),  $S_c$  is larger than the effective polar cap radius  $r_{pc,E} = r_{pc} R_{E,6}^{3/2}$ . The gap shape becomes narrow and long. The boundary conditions at the open field line boundaries become important, so that  $(\nabla \cdot \mathbf{E})_{\parallel}/(4\pi)$  can be much less than  $(\nabla \cdot \mathbf{E})/(4\pi)$ . The approximation (65) no longer holds. To achieve a very accurate description of such reversed positron fraction, one has to appeal to complicated mathematical descriptions (e.g. Muslimov & Tsygan 1992; HM98) or numerical simulations to get  $(\nabla \cdot \mathbf{E})_{\parallel}/(4\pi)$ . However, noticing that  $(\nabla \cdot \mathbf{E})_{\parallel}/(4\pi) \simeq (\nabla \cdot \mathbf{E})/(4\pi) \simeq \partial E_{\parallel}/\partial r$ , we can still get an approximate formula for  $f$  by adopting (A4) of HM98, and making some reasonable simplification, which finally reads

$$f(\text{II}) \simeq 3\kappa_0(1-\xi^2) \left[ \frac{f(\eta)}{f(\eta_*)} \right]^{-3} (1-\eta_*^2 \frac{\kappa}{\eta^3})^{-1} r_{e,6}^{-2} R_{E,6}^3 \left( \frac{\Omega R}{c f(1)} \right) \\ \simeq 5.7 \times 10^{-5} r_{e,6}^{-2} R_{E,6}^3 P^{-1}, \quad (71)$$

where the function  $f(\eta)$  is the correction factor of the polar cap radius in curved spacetime (see eq.[8] of HM98), which is equivalent to the function  $q(r)$  introduced in this paper (see eq.[19]). Other notions have been described above, and typical values have been adopted. With eqs.[68,64,60,71], it is easy to estimate the polar cap heating luminosity in regime II,

$$L_{x,pc,max}(\text{II}) \simeq 9.1 \times 10^{26} \text{erg} \cdot \text{s}^{-1} B_{p,12} P^{-13/4} r_{e,6}^{-2} R_{E,6}^5 (\cos \alpha)^{5/4}, \quad (72)$$

and the polar cap temperature

$$T_{pc,max}(\text{II}) \simeq 0.53 \times 10^6 \text{K} B_{p,12}^{1/4} P^{-9/16} r_{e,6}^{-1/2} R_{E,6}^{5/4} (\cos \alpha)^{5/16}. \quad (73)$$

We see that  $T_{pc,max}(\text{II})$  is sensitive to pulsar period ( $\propto P^{-9/16}$ ) while  $T_{pc,max}(\text{I})$  is not ( $\propto P^{-1/14}$ ). This is just the refraction of the open field line boundary conditions

on the saturated gap. We also notice that the peak energy of such thermal emission falls into the ROSAT band. However, it is notable that the thermal X-ray luminosity (eqs.[69] or [72]) does not have the dependence that is observed in ROSAT band ( $L_x(\text{ROSAT}) \propto L_{sd}$ , BT97). This rules out the possibility of interpreting ROSAT luminosities in terms of only thermal emission due to polar cap heating. We will show next, however, that a combination of such thermal luminosities with the non-thermal luminosities due to the ICS of higher generation pairs could roughly reproduce such dependence. The thermal component discussed above will dominate the ROSAT band emission in most of the millisecond pulsars. Another point is that, the luminosity and polar cap temperature formulae presented above (eqs.[69,70,72,73]) are still upper limits, especially for the saturated regime (regime II), though actual values are not much lower. For the millisecond pulsars which are near the deathlines (Zhang et al. 1999), such deviations could be even larger, since our approximations adopted to describe the accelerator are no longer accurate enough.

### 3.3. Non-thermal X-ray luminosity

In our full-cascade picture, we can naturally get a non-thermal X-ray emission component from the soft tail of the ICS spectra of the higher generation pairs. Attaining an accurate spectrum requires a more careful modeling using Monte Carlo simulation approach, which will not be done in this paper. However, some simple estimate of the non-thermal X-ray luminosities of pulsars could be achieved using the analytic method described in Sect.2.3 and 2.4.

Let us compute the luminosity below a certain energy  $E_c$ . In principle, one should add the contributions from all the branches over the whole cascades. However, it is notable that the SR spectra of all the SR branches can not get down to as low energy as the X-rays observed by ROSAT and ASCA (Harding & Daugherty 1999; Rudak & Dyks 1999). This could be justified as follows. The lowest characteristic SR energy in the full-cascade is

$$E_{c,\min}(\text{SR}) = E_0 \kappa_{\text{SR}}^{\zeta_{\text{SR}}}, \quad (74)$$

and in principle, the minimum SR energy is the blueshifted cyclotron energy (corresponding to the electron occupying only one Landau state, see Harding & Daugherty 1999)

$$E_{\min}(\text{SR}) = \gamma_{\zeta_{\text{SR}},\parallel} \hbar \omega_{B,e} = \gamma_{\zeta_{\text{SR}},\parallel} m c^2 B_e', \quad (75)$$

where

$$\gamma_{\zeta_{\text{SR}},\parallel} = \frac{\epsilon_0 \kappa_{\text{SR}}^{(\zeta_{\text{SR}}-1)}}{2} \eta_{\parallel} \quad (76)$$

is the initial parallel energy of the last generation ( $\zeta_{\text{SR}}$ -th generation) pairs.

For a typical normal pulsar with  $P = 0.1\text{s}$ ,  $B_{p,12} = 5.8$  (thus  $B_{e,12} \simeq B_{p,12} R_{E,6}^{-3} = 1$  for  $R_{E,6} = 1.8$ ), and  $\alpha = 30^\circ$ , we have  $E_0 \sim 196\text{GeV}$  (eq.[48]),  $E_{\text{esc}} = 0.52\text{GeV}$  (eq.[28]),  $\kappa_{\text{SR}} \sim 1/16$  (eq.[32]),  $\zeta_{\text{SR}} = 3.14$  (eq.[44]), and  $\eta_{\parallel} = 0.237$  (eq.[38]), so that  $E_{c,\min}(\text{SR}, \text{nPSR}) \sim 32.8\text{MeV}$  and  $E_{\min}(\text{SR}, \text{nPSR}) = 1.26\text{MeV}$ . Both values are much higher than the X-ray bands we are interested in (e.g. below  $10\text{keV}$ ). Similarly, for a typical millisecond pulsar with  $P \sim 0.005\text{s}$ ,  $B_{p,9} = 0.5$ ,  $R_{E,6} = 1.2$ , and  $\alpha = 30^\circ$ , we have  $E_0 \sim 163\text{GeV}$  (eq.[51]),  $E_{\text{esc}} = 159\text{GeV}$  (eq.[29]),

$\kappa_{\text{SR}} \sim 1/11$  (eq.[33]),  $\zeta_{\text{SR}} = 1.01$  (eq.[44]), and  $\eta_{\parallel} = 1.6 \times 10^{-5}$  (eq.[39]), so that  $E_{c,\text{min}}(\text{SR, msPSR}) \sim 149\text{GeV}$  and  $E_{\text{min}}(\text{SR, msPSR}) = 0.026\text{KeV}$ . Note although the lowest end of this SR spectra could be down to as low as  $0.026\text{KeV}$ , there is a very wide span of energy of the last SR generation starting from more than  $100\text{ GeV}$ . Thus the SR contribution to the ASCA and ROSAT band X-rays is tiny compared to the ICS contributions as described below.

For the ICS branches, the expression of characteristic energy (eq.[34]) is similar to the minimum SR energy (eq.[75]), but the physical meaning is different (see Sect.2.3). The most important difference is, as long as the resonant scattering condition (eq.[4]) is satisfied, the Lorentz factor of the pairs will keep decreasing so that the characteristic energy of the ICS process will cover a broad energy range, the low energy end of which could present a significant contribution to the X-ray band we are interested in.

As described above, the complication of the full-cascade picture makes it difficult to obtain an analytic expression which includes all the possible contributions to the X-ray luminosity. The main complication arises from the ‘‘mixed’’ generations. However, there are two essential features that make such an analytic expression possible: (1) The energy distribution to the two branches is fixed for a certain pulsar (e.g.  $\eta_{\perp}$  and  $\eta_{\parallel}$  are constant for a certain pulsar regardless the generation order, see eqs.[37,40]) if we ignore the small variation of  $B_e$  in the different generations; (2) Only ICS branches can have significant contributions to X-ray luminosities. In principle, The upper limit of the non-thermal X-ray luminosity below a certain energy  $E_c$  could be estimated as

$$L_{x,\text{nth}}(E_c) \lesssim L_{\text{pc}} \sum_{k=1}^{\text{int}(\zeta_{\text{SR}})} \left[ \eta_{\perp}^{k-1} \left( \sum_{j=1}^{\text{int}(\zeta_{\text{ICS},k-1})} \eta_{\parallel}^j \eta_{c,k,j} \right) \right]. \quad (77)$$

Here  $\zeta_{\text{SR}}$  is just the pure SR generation order parameter defined in (44), and  $\zeta_{\text{ICS},k}$  is some more general ICS generation order parameter defined by

$$\zeta_{\text{ICS},k} = \frac{\log(E_{\text{esc}}/E_k)}{\log(\kappa_{\text{ICS}})} + 1, \quad (78)$$

which is the number of pure ICS generations for the typical energy of the  $k$ -th SR generation,

$$E_k = E_0 \kappa_{\text{SR}}^k, \quad (79)$$

to reduce to the escaping energy  $E_{\text{esc}}$  (eqs.[28, 29]). Note that we have defined that, for  $k = 0$ ,  $E_k$  is just  $E_0$  (eqs.[48] or [51]). To keep consistency with (44) and (45), we still keep the term (+1) in (78), but use  $(k - 1)$  in (77) and (81) to subtract this extra generation. Another important parameter in (77),  $\eta_{c,k,j}$ , is to describe the portion of the particles’ energy that goes to the band below certain  $E_c$  in a certain ICS branch, which is defined as the ratio of the Lorentz factor required to produce ICS photons with energy  $E_c$ ,

$$\gamma_c = E_c / [(1 - \beta u) 2.8kT], \quad (80)$$

to the initial parallel Lorentz factor of particles from the  $(j - 1)$ -th ICS-photon-produced pairs from the  $(k - 1)$ -th

SR-photon-produced pairs,

$$\gamma_{k,j} = \frac{\epsilon_0 \kappa_{\text{SR}}^{k-1} \kappa_{\text{ICS}}^{j-1}}{2} \eta_{\parallel}, \quad (81)$$

so that

$$\eta_{c,k,j} = \begin{cases} 1, & \gamma_c \geq \gamma_{k,j} \\ \gamma_c / \gamma_{k,j}, & \gamma_c < \gamma_{k,j} \end{cases}, \quad (82)$$

and the truncation of  $\eta_{c,k,j} = 1$  at  $\gamma_c \geq \gamma_{k,j}$  ensures the energy portion can not exceed 100%. Note that (77) has included most of the branches that have contributions to the X-ray luminosity. There are still some branches missing, e.g., the ICS branch from the SR branch produced by the even earlier ICS branch. In any case, the correction of these ‘‘higher order’’ branches to (77) is tiny.

The estimate in (77) actually involves the assumption that the conversion efficiency from particle kinetic energy to radiation in the ICS branches is 100%. This is only true when the resonant scattering condition (4) is fulfilled. If the resonant condition fails, the estimate in (77) is then just an upper limit. Thus it is essential to compare  $\gamma_{\text{res}}$  (eq.[4]) with  $\gamma_c$  (eq.[80]). If  $\gamma_{\text{res}} \ll \gamma_c$ , the ICS processes producing photons with  $E_c$  are well within the resonant regime, then  $\eta_{c,k,j}$  is essentially the precise energy portion. If  $\gamma_{\text{res}} \sim \gamma_c$ , the ICS processes can still produce photons with  $E_c$ . But the process just marginally occurs in the resonant regime, thus  $\eta_{c,k,j}$  is a marginal upper limit. If, however,  $\gamma_{\text{res}} \gg \gamma_c$ , the resonant scattering has stopped at a much higher energy than  $\gamma_c$ . Then only a small portion of the photons with  $E_c$  could be produced, then  $\eta_{c,k,j}$  could just be regarded as a very loose upper limit. Such differences are reflected in Table 3. Note that when calculating the X-ray luminosity within a certain band,  $E_{c1} < E < E_{c2}$ , we have actually taken  $L_{\Delta E} = L_{x,\text{nth}}(E_{c2}) - L_{x,\text{nth}}(E_{c1})$  as the predicted luminosity in this band. In Table 3, we have adopted ‘ $\sim$ ’, ‘ $\lesssim$ ’, and ‘ $<$ ’, for the cases of  $\gamma_{\text{res}} \leq \gamma_{c1}$ ,  $\gamma_{c1} \leq \gamma_{\text{res}} \leq \gamma_{c2}$ , and  $\gamma_{\text{res}} > \gamma_{c2}$ , respectively. For old normal pulsars such as PSR 1929+10 and PSR 0950+08, since both the cooling temperature (62) and the polar cap temperature (73) are much lower, the ICS efficiency is lower. Unless  $\gamma_{\text{res}} \leq \gamma_{c1}$ , we will adopt  $<$  since the actual luminosity could be much lower than the predicted upper limits.

The complicated form in equation (77) could be simplified for the pulsars in which pair production from ICS photons are not important. This is the case for most pulsars except the ones with high  $B$  (Table 2). For  $\zeta_{\text{ICS},k} < 2$ , equation (77) turns out

$$L_{x,\text{nth}}(E_c) \lesssim L_{\text{pc}} \sum_{k=1}^{\text{int}(\zeta_{\text{SR}})} (\eta_{\perp}^{k-1} \eta_{\parallel} \eta_{c,k,1}). \quad (83)$$

In our calculation, we have adopted (77) uniformly without losing generality, and used (83) to do the comparison. We found that, for high  $B$  pulsars, the luminosity from (77) is much higher than the one from (83), which means that the higher order generations have important contributions to these pulsars.

The use of (77) for the millisecond pulsars is not accurate. This is because, for millisecond pulsars, we have  $\gamma_c > \gamma_{1,1}$ . In other words, the maximum emission energy

of the first ICS-branch (i.e. the ICS-branch from the secondary pairs) has dropped below the ASCA and ROSAT band. This can be understood by noting the very small  $\eta_{\parallel}$  (msPSR) (eq.[39]) and  $\kappa_{\text{ICS}}$  (msPSR) (eq.[43]). Thus using (77) will underestimate the non-thermal X-ray luminosities. To amend this, we introduce a separate formula for millisecond pulsars

$$L_{x,nth}^{\text{msPSR}}(E_c) \lesssim L_{\text{pc}} \sum_{k=1}^{\text{int}(\zeta_{\text{SR}})} (\eta_{\perp}^{k-1} \eta_{\parallel}^{\zeta_{c,k-1}}), \quad (84)$$

where  $\zeta_{c,k}$  is defined by

$$\zeta_{c,k} = \begin{cases} 0, & E_c \geq E_k \\ \frac{\log(E_c/E_k)}{\log \kappa_{\text{ICS}}}, & E_c < E_k \end{cases}, \quad (85)$$

$E_c$  is the energy we are interested in, and  $E_k$  follows (79).  $\zeta_{c,k}$  is the number of the ICS generations with which the typical emission energy is dropped to  $E_c$  from  $E_k$ . For millisecond pulsars, this value is smaller than unity. Thus equation (84) can raise the X-ray luminosity estimate a little bit compared with (77) or (83). Note again the adoption of  $<$ ,  $\lesssim$  or  $\sim$  is pending on the resonant condition.

Finally, we should notice another general relativistic effect, i.e., the redshift of the photons, when comparing the theoretical predictions with the observations. More specifically, the energy of interest  $E_c$ , which is used in above calculations, is connected with the observational energy  $E_{\text{obs}}$  by a redshift factor:

$$E_c = (1 - \frac{r_g}{r_e})^{-1/2} E_{\text{obs}} \simeq (1 - 0.4r_{e,6}^{-1})^{-1/2} E_{\text{obs}}. \quad (86)$$

The redshift correction factor  $(1 - \frac{r_g}{r_e})^{-1/2}$  is 1.13 for  $r_{e,6} = 1.8$  and 1.29 for  $r_{e,6} = 1$ . By adopting  $E_{\text{obs}} = 0.7 - 10\text{keV}$  and  $0.1-2.4\text{keV}$ , we can then calculate the (maximum) non-thermal X-ray luminosities for the ASCA and ROSAT bands, respectively.

### 3.4. Results

We have performed detailed calculations of the predicted non-thermal and polar cap heating thermal X-ray luminosities of all the known X-ray pulsars detected by ROSAT or ASCA. In Table 2, we listed the model parameters of these 35 pulsars, which are separately grouped into normal and millisecond pulsars. Table 3 shows the calculation results of both the thermal and non-thermal X-ray luminosity predictions of the known X-ray pulsars and the comparison with the observational data (BT97 and S98). The model prediction for the total ROSAT band is a sum of the ICS-origin non-thermal luminosity ([77] or [84]), the thermal luminosity due to polar cap heating ([69] or [72]), and the cooling thermal luminosity by assuming  $R = 10^6\text{cm}$  for all the pulsars. This is because the predicted peak thermal components usually fall into the ROSAT band. For non-thermal luminosity both for ROSAT and ASCA bands, we use (77) for all the normal pulsars, and use (84) for all the millisecond pulsars. Unless the temperature data are available from data analysis ( $T_{s,6} \sim 1.5$  for Vela, Ögelman et al. 1993;  $T_{s,6} \sim 0.56$  for Geminga, Halpern & Wang 1997;  $T_{s,6} \sim 0.8$  for both PSR 0656+14 and PSR 1055-52, Greiveldinger et al. 1996, Wang et al. 1998), we have

adopted the values of  $T_{s,6}$  and  $T_{h,6}$  according to (62) and (70) or (73). For other model parameters, we have adopted  $\xi = 1$  (the last open field line),  $\alpha = 30^\circ$  for all the pulsars,  $R_{E,6} = 1.8$  for most of the normal pulsars,  $R_{E,6} = 1.5$  for the relatively old normal pulsars (PSR 0950+08 and PSR 0823+26) and  $R_{E,6} = 1.2$  for the the millisecond pulsars. Such adoptions for  $R_{E,6}$ , though rough, are based on the numerical results of HM98 (their Fig.10). The weak dependence of  $R_{E,6}$  on pulsar parameters like  $P$ ,  $B_p$  and  $T$  is the main reason for us to adopt fixed values of  $R_{E,6}$  for different groups of pulsars. In principle, for normal pulsars,  $R_{E,6}$  is not a free parameter, since it is determined by  $T_{h,6}$  and the pulsar parameters ( $P$ ,  $B_{p,12}$  and  $\cos \alpha$ ), and  $T_{h,6}$  itself is also the function of  $P$ ,  $B_{p,12}$  and  $\cos \alpha$  (see eqs.[70] or [73]) if we assume the polar cap heating is the only process to decide polar cap temperature. However, the complication of the processes prevents an analytic expression of

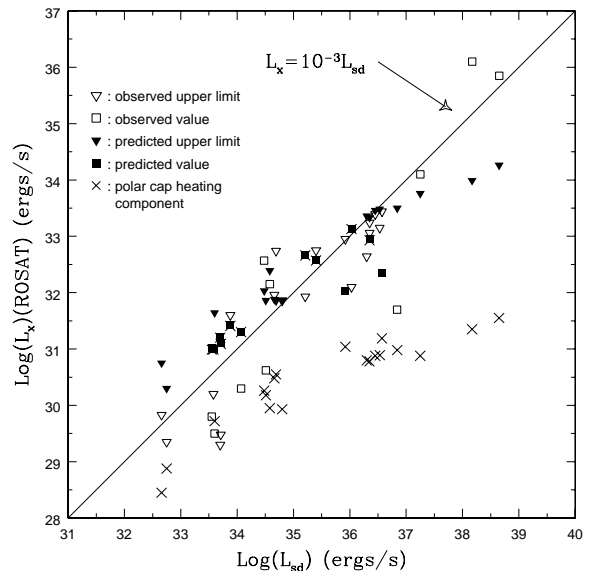


FIG. 4.— Comparison of the luminosities observed and predicted in the ROSAT band for 29 pulsars. Note upper limits are adopted for some pulsars both for the observational and theoretical values. Note how  $L_x(\text{ROSAT}) \propto L_{\text{sd}}$  feature is well reproduced, and how the thermal component due to polar cap heating dominates the luminosity in millisecond pulsars.

The X-ray luminosity predictions versus observations are plotted in Fig.4 and Fig.5. If a pulsed signal is detected for a certain source, we have adopted the *pulsed* emission luminosity as the observational value, since we believe that only this luminosity is relevant to what we are discussing in this paper. For the detections without pulsed signals, we adopt their luminosities as upper limits. For the theoretical results, we adopt the sum of both the thermal and non-thermal X-ray luminosities for the ROSAT band, but only non-thermal luminosity for the ASCA band. We regard both the values marked with ‘ $\sim$ ’ and ‘ $\lesssim$ ’ in Table 2,3 as the actual values, while the values marked with ‘ $<$ ’ as upper limits to plot Fig.4 and Fig.5. It is notable from Fig.4 that, a  $L_x(\text{ROSAT}) \propto L_{\text{sd}}$  feature is roughly reproduced, and the thermal component due to polar cap heating clearly dominates the ROSAT band luminosities

of the millisecond pulsars. The comparison of the theoretical predictions with the ASCA observations (S98, Saito et al. 1998) is less satisfactory, but not in strong conflict when one bears in mind the small sample and large uncertainties in the ASCA data. Furthermore, the inconsistency could be weakened by adjusting free parameters like  $\alpha$  and  $R_{E,6}$ .

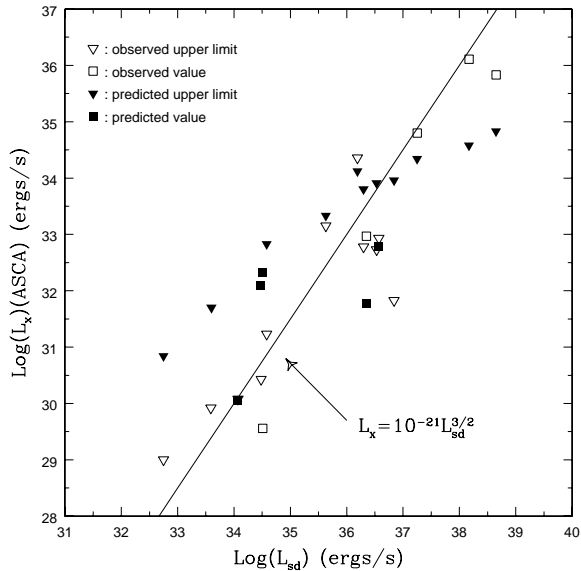


FIG. 5. — Comparison of the luminosities observed and predicted in the ASCA band for 15 pulsars. Notations are same as those adopted in Fig.4.

In Fig.6 and Fig.7, we plotted the dependence of our model predictions on the free parameters  $\alpha$  and  $R_{E,6}$ . We see both the  $\gamma$ -ray and X-ray luminosities are mildly decreasing when  $\alpha$  gets larger. The decreasing becomes prominent when  $\alpha$  gets closer to  $90^\circ$ . However, one should notice that such decreasing can not get too low (say, below 2 orders of magnitudes), since the smaller  $\sin \alpha$  term, which has been neglected in writing down the parallel electric fields in the HM98 model, will become important for  $\alpha \sim 90^\circ$ . The dependences of the non-thermal X-ray luminosity on  $R_{E,6}$  or  $\alpha$  are not smooth (Fig.6a,7a,7b). This is expected since the zigzags actually reflect the contributions from different ICS branches. For different adoptions of  $R_{E,6}$  or  $\alpha$ , the significance of the contributions of certain ICS branches to the final luminosity in a certain band actually varies. Thus the zigzag features are real physical effects. However, we notice that there exist several non-differentiable points in the curves. This is an artifact, which arises from the truncation features in (82). We believe that the detailed numerical simulations can smooth out these non-differential points, though the small “bump” features should remain. The present estimate could bring some errors near these non-differential points. For the millisecond pulsars, the height dependence is simpler (Fig.7b), mostly because the generation structure is simpler (both  $\zeta_{SR}$  and  $\zeta_{ICS}$  are smaller than 2), and also due to the non-integer description (84).

#### 4. CONCLUSIONS AND DISCUSSIONS

#### 4.1. Conclusions

We have modified the conventional CR(or ICS)-SR polar cap cascade picture by including the contributions of the ICS photons produced by the higher generation pairs within the framework of the space-charge-limited flow acceleration model proposed by Harding & Muslimov (HM98). Such a full-cascade picture is more complicated than the canonical model. The complications mainly result from the two-branch feature of the cascade, and the different regimes of the ICS process under different conditions. The important parameters, i.e., the temperatures of both the full surface and the hot polar cap, are still uncertain since there are many other factors (besides cooling and polar cap heating) that can influence them. The uncertainty of the temperatures will bring uncertainties of the “resonant ICS condition” (eq.[4]), the height of the accelerator  $R_{E,6}$ , etc., and thus bring uncertainties to our model predictions. Furthermore, the complication of the accelerator itself (HM98) has already been difficult to delineate analytically. Therefore, to achieve a more accurate prediction, one has to appeal to detailed Monte Carlo simulations. However, some interesting features, e.g. the resonant condition is satisfied for a wide range of parameters;  $R_{E,6}$  does not sensitively depend on pulsar parameters; the field strength variation is not important within generations; only ICS branches have notable contributions to X-ray luminosities; and so on, make an analytic description of the process possible. We have tried to treat the process as accurately as possible so as to keep as much information as we could. Such efforts include the correction of the general relativistic effects (enhancement of the field strength and photon energy redshift); the correction of the non-zero pitch angle effect for higher SR generations; more accurate and separate adoptions of the critical  $\chi$  for describing the cascade and escaping processes; separate treatments of the normal and the millisecond pulsars, and so on. As shown in the previous sections, our analytic description has presented an overview to the high energy emission features of the pulsar population. Our main findings in this paper can be summarized as follows:

1. When high energy photons are converted to pairs in the pulsar magnetosphere via  $\gamma - B$  process, not only the perpendicular energy of the pairs are further converted into radiation via SR, most of the parallel energy of the pairs will be also converted to radiation via the ICS of the particles with the soft thermal photons. Thus there is almost no energy loss during the conversion of the accelerating particle energy to radiation in the cascade process. Such a full-cascade scenario gives a natural interpretation to the  $L_\gamma \propto (L_{sd})^{1/2}$  feature.

2. SR branches of the cascade have little contribution to the X-rays in the ROSAT and ASCA bands. The ICS-branch spectra, however, can result in a non-thermal X-ray component with their soft tails. Such non-thermal X-rays of ICS-origin play an important role to account for the ROSAT and ASCA luminosities.

3. The polar cap heating from backflowing particles of the inner accelerator can contribute a hot thermal component with small area (e.g. polar cap), which also has a contribution to the ROSAT luminosity.

4. The combination of the thermal and the non-thermal components in the model reproduces the re-

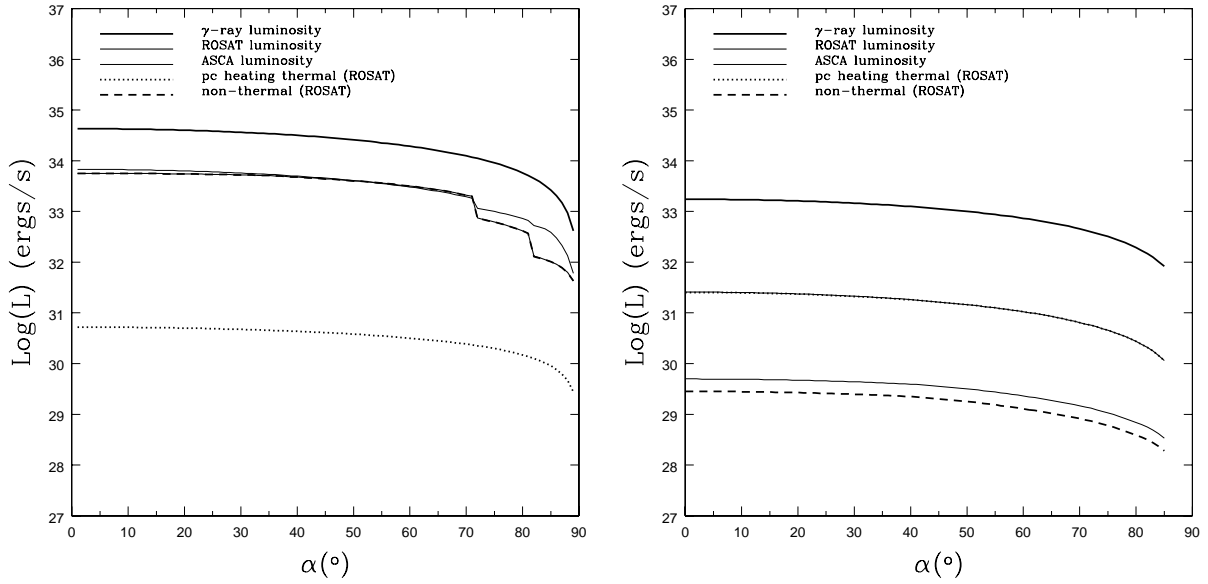


FIG. 6.— The inclination angle ( $\alpha$ ) dependence of the predicted luminosities. (a) for a normal pulsar:  $P = 0.1\text{s}$ ,  $B_{p,12} = 5.8$ ,  $r_{e,6} = 1.8$ , note ROSAT luminosity is dominated by the non-thermal component; (b) for a millisecond pulsar:  $P = 0.005\text{s}$ ,  $B_{p,12} = 5 \times 10^{-4}$ ,  $R_{E,6} = 1.2$ , note ROSAT luminosity is dominated by the thermal component.

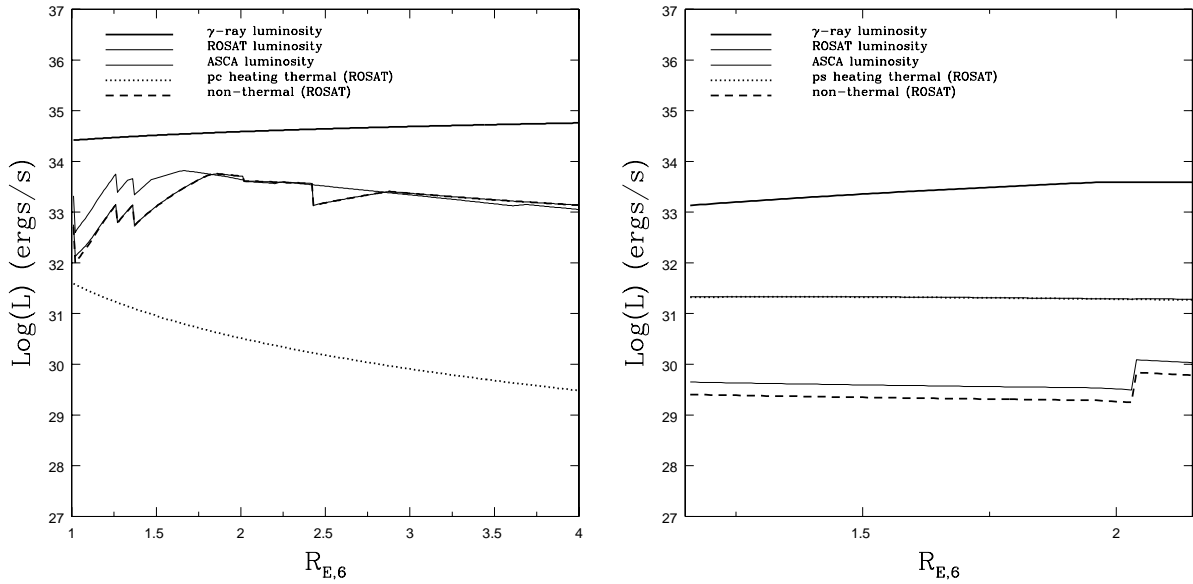


FIG. 7.— The emission height ( $R_{E,6}$ ) dependence of the predicted luminosities. (a) For a normal pulsar:  $P = 0.1\text{s}$ ,  $B_{p,12} = 5.8$ ,  $\alpha = 30^\circ$ . b) For a millisecond pulsar:  $P = 0.005\text{s}$ ,  $B_{p,12} = 5 \times 10^{-4}$ ,  $\alpha = 30^\circ$ . The zigzags indicate the contributions from different ICS branches. Note also that the ROSAT luminosity is dominated by the non-thermal component for normal pulsars, but by thermal component for millisecond pulsars.



ported  $L_x(\text{ROSAT}) \sim 10^{-3}L_{\text{sd}}$  feature (BT97). The non-thermal components predicted in the ASCA band is not in severe contradiction to the ASCA data (S98).

5. For the ROSAT band, the non-thermal components dominate the luminosities for all the normal pulsars, while the upper limits of the thermal luminosities are usually higher than the non-thermal luminosities for the millisecond pulsars. We thus predict that the unidentified spectral features of the *pulsed* emission of the millisecond pulsars might be of thermal origin.

Zhang & Harding (1999) have also presented similar conclusions. The main improvement of this paper is that we have included both the unsaturated and the saturated cases of the space-charge-limited flow accelerators.

#### 4.2. Comparisons with the outer gap model

The  $L_x \sim 10^{-3}L_{\text{sd}}$  feature has been also interpreted in terms of the thick outer gap model by Cheng et al. (CGZ98; CZ99), thus it is of interest to compare our model with the outer gap model. The main differences between the two models lie in the following aspects:

1. We interpret the non-thermal X-rays as being due to the ICS of upward polar cap cascades, while the outer gap model attributes the non-thermal X-rays to the SR of the downward cascades from the outer gap particles. A prominent feature of our model is that we can simultaneously reproduce both the observed  $L_\gamma \propto (L_{\text{sd}})^{1/2}$  and the  $L_x \sim 10^{-3}L_{\text{sd}}$  dependences well. The thick outer gap model, however, has a quite different  $L_{\text{sd}}$ -dependence of the  $\gamma$ -ray luminosities ( $L_\gamma \propto B_{p,12}^{2/7} P^{-2/7}$ , see a combination of eqs.[23], [22] of Zhang & Cheng 1997) which severely violates the observed  $L_\gamma \propto (L_{\text{sd}})^{1/2}$  dependence, although  $L_x \sim 10^{-3}L_{\text{sd}}$  feature was also well reproduced.

2. As for the thermal X-rays, our model predicts a hot small area component in terms of polar cap heating, and adopt the full-surface temperature from a simple cooling model. In the outer gap model, both the full-surface and the polar cap temperatures are predicted in terms of the thick outer gap heating (Zhang & Cheng 1997; CGZ98; CZ99). CZ99 also took into account the possible effect of the polar cap heating in old pulsars PSR 1929+10 and PSR 0950+08, in which the outer gap might not be formed. An important difference is that, for our model, as long as the resonant condition (4) is satisfied, our model predictions are not sensitively dependent on the surface temperatures, while in the outer gap model, the surface temperatures are closely related to the non-thermal X-ray luminosities due to the self-consistency of the model.

3. In the pure non-thermal-origin outer gap model (CGZ98), some direct analytic expressions of the soft X-ray luminosities in terms of the spin-down energy (their eqs.[15,16]) are available. However, such a model is incomplete since the thermal emission should have a non-negligible contribution to the ROSAT band emission, and such thermal components have indeed been identified from some pulsars (see Sect.1). CZ99 improved the model by incorporating the thermal contributions. But they assumed that the hard polar cap thermal components do not have a significant contribution to the ROSAT observations. Their results combining both the non-thermal and the soft full-surface thermal components can also reproduce the  $L_x(\text{ROSAT}) \sim 10^{-3}L_{\text{sd}}$  feature. In our polar

cap model, a simple expression for the hot thermal luminosity ([69] or [72]) is available, but no simple analytic expression (in terms of pulsar parameters) could be achieved to describe the non-thermal luminosity due to complexity of the cascade processes. A sum of both the thermal and non-thermal luminosities can also result in a rough  $L_x(\text{ROSAT}) \sim 10^{-3}L_{\text{sd}}$  dependence. The distinguishing point between the two models might be the different origin of the soft X-rays from the millisecond pulsars. As addressed above, our model predicts that the pulsed emission of the ROSAT-observed millisecond pulsars might be dominated by the thermal component due to polar cap heating, while the outer gap model attributes the millisecond pulsar soft X-rays also to the non-thermal SR component, although they adopted an additional assumption of strong multipole magnetic field components for these pulsars. Such an issue could be a discriminator between the two models. Unfortunately, among the 10 X-ray millisecond pulsars, spectral analyses are only performed on two pulsars. Although there is evidence of the existence of a hot thermal component in PSR J0437-4715 (Becker & Trümper 1993; Halpern, Martin & Marshall 1996; Zavlin & Pavlov 1998), a combination of the ROSAT and ASCA data shows that the spectrum of PSR B1821-24 is a power-law, and thus, of non-thermal origin. According to our results (Table 3), the observational values both in ROSAT and ASCA band for PSR 1821-24 are much higher than model predictions, and also much higher than the observed values of other millisecond pulsars. This leads us to suspect that there might be some special non-thermal X-ray emission mechanisms operating in this pulsar. Thus, when more data are accumulated, the spectral analyses of the pulsed emission of the other millisecond pulsars could provide evidence for or against our idea. It is worth noticing that the thermal feature for the millisecond pulsars is also expected by Zavlin & Pavlov (1998). However, if there indeed exist strong multipole magnetic fields near a millisecond pulsar's surface, the differentiating between the models becomes difficult, since our model also predicts much stronger non-thermal emission components due to the enhancement of the ICS emission efficiency.

4. Among 35 detected spin-powered X-ray pulsars, pulsed emission components are only observed in 10 pulsars by ROSAT, 4 of which (Crab, Geminga, PSR B1509-58 and PSR B0540-69) are also observed by ASCA. ASCA also observed pulsed strong non-thermal emission from another pulsar, the millisecond pulsar PSR B1821-24. For other pulsars, only the total X-ray luminosities are reported. Our polar cap model actually predicts pulsed emission luminosities. Thus, as long as the pulsed luminosity is detected, we use it to compare with the model prediction. For those pulsars in which no pulsed emission is detected, we regard the total luminosity as an upper limit (see Fig.4,5), since besides the internal (cooling and heating) and magnetospheric (polar cap or outer gap heating, and ICS or SR non-thermal emission) origin X-rays, there are still many mechanisms, such as the accretion from the interstellar medium (Paczynski 1990), pulsar wind nebular emission (Arons & Tavani 1993), etc., which can account for non-pulsed X-ray emission. We noticed that, however, in the outer gap model, the total luminosities are adopted to compare with the model predictions. On the theoretical aspect, the outer gap model predicts a precise value,

but our model predictions could either be a actual value or an upper limit pending on whether the ICS occurs in the resonant regime (see Table 3; Fig.4,5). More precise predictions will be available after detailed numerical simulations.

5. Besides the spectral behavior of the millisecond pulsars, another issue could also be regarded as a differential criterion of the competing models. For the relatively old canonical pulsars such as PSR 0950+08 and PSR 1929+10, the outer gap model predicts pure thermal emission (due to polar cap heating), since outer gaps could not be formed in these pulsars (CZ99). Our model, however, predicts a non-thermal plus thermal feature. The thermal emission component due to polar cap heating has a luminosity comparable to the ICS-origin non-thermal component, so that both of them are detectable.

#### 4.3. Further remarks

We have some further remarks on our model. Firstly, the analytic description approach adopted in this paper has some limitations in presenting detailed predictions. As shown in Sect.2.3, when deducing the recursion relations between adjacent generations, we have only examined the characteristic emission energies, but ignored the detailed radiation spectrum of each generation. This is the main reason for the non-smooth features in Fig.7a. Furthermore, the expressions of the predicted luminosities may need further revisions to include more effects that might be important. For example, in (77), one may need to incorporate a weighting factor to describe the  $\gamma$ -dependence of  $\dot{\gamma}$ , since (77) assumes equal number density for the particles with different  $\gamma$ s, which might not be necessarily the case. Therefore to get detailed  $\gamma$ -ray and X-ray spectra, careful numerical simulations are desirable. Nevertheless, we can give a rough estimate of the non-thermal X-ray spectral indices. According to Dermer (1990), the thick-target magnetic ICS spectral indices are approximately  $1 + \Gamma/2$  or  $\Gamma$  within different energy regimes (see his eqs.[41a,41b]), where  $\Gamma$  is the spectral index of the stable input particle spectrum. Monte Carlo simulation results (DH96) show that for the higher generation pairs, usually one has  $\Gamma \sim 1.5 - 2$ , so that the final photon spectral indices are around  $1.75 - 2$ . This is in good agreement with the observations (BT97).

Our present model is not good at describing the high magnetic field pulsars. Although we have tried to accommodate high  $B$  pulsars by including higher order ICS branches (eq.[77]), there are still several aspects of high  $B$  pulsars that we did not take into account. First, the model predictions presented in this pulsar are mainly very loose upper limits rather than actual values. This is because, for high  $B$  pulsars, the cyclotron energy is very high. The typical Lorentz factor for the resonant ICS condition (eq.[4]) is thus also very high (e.g.  $\sim 10^3$ ), and is much higher than the Lorentz factor (e.g. about 100) required to emit soft X-rays in the ROSAT or ASCA bands. Thus the electrons may not be able to reduce their energies enough to scatter the soft photons to these bands, so that in some cases, the pulsar may not be detected in X-rays at all. Another point is that in high  $B$  pulsars, the accelerator should be controlled by ICS, since both the upward and downward scatterings occur in the resonant regime, and the anisotropy of the ICS processes no longer exist. The

accelerator is hence moved back to the vicinity of the surface ( $R_{E,6} = 1$ ), and the expression of  $E_0$  ([48] or [51]) should be modified by the ICS-controlled one. All these will alter the generation structures of the high  $B$  pulsars, and change the model predictions to some extent. Furthermore, photon splitting is also important for high  $B$  pulsars (HBG97), and will complicate the cascade picture even more. Thus to compute the cascade spectrum of these high  $B$  pulsars, one has to appeal to rather complicated numerical simulations (see e.g. Baring & Harding 1999).

Though with limitations, the analytic approach adopted in this paper has its advantage to present a general overview of the emission properties of different pulsars without performing detailed numerical simulations. For example, our model shows that, for most young pulsars, the non-thermal luminosities are much higher than both the full-surface and the hot polar cap thermal luminosities, so that the thermal components should be buried by the non-thermal power law continuum. For some middle-aged pulsars such as Geminga, PSR 0656+14, and PSR 1055-52, however, the predicted non-thermal X-ray luminosities are of the same order of the full-surface thermal luminosities, thus these thermal components could be detectable. This is just what is observed. Another example is that our model seems to have the ability to interpret some ‘‘missing detections’’. For example, ROSAT has detected 10 millisecond pulsars. If pulsar X-rays for the millisecond pulsars are indeed of non-thermal origin as the outer gap model argued, then most of them should be detected by ASCA as well, since the ASCA’s band is higher and wider. However, only 2 out of those 10 are detected by ASCA. In our model, the ROSAT-band emission for these millisecond pulsars is dominated by the thermal emission, which is stronger than the non-thermal component. In the ASCA band, only the non-thermal component is present, so that the predicted luminosities are lower. In fact, our predictions of the ASCA luminosities of these 10 millisecond pulsars are usually too low to be detected (see Table 3) except for PSR B1821-24, which has been indeed observed to be dominated by the non-thermal emission though our prediction is still less by almost an order of magnitude. For PSR J0437-4715, we predicted a low luminosity in ASCA band, which is close to the observational level. The detection of this pulsar by ASCA is due to the close distance of the source. Another example of the ‘‘missing detections’’ is, among the ASCA detected 16 pulsars (S98), only two pulsars, i.e., PSR B1610-50 and PSR 1853+01, were not detected by ROSAT. This is not easy to be understood in terms of the outer gap model. In our model, we can present a simple interpretation. We noticed that these two pulsars all have the magnetic fields higher than  $10^{13}$ G. The absence of soft X-rays from these two pulsars might just be due to the failure of the resonant scattering condition in the ROSAT band as discussed above. However, some other high  $B$  pulsars, e.g. PSR B1509-58 and PSR B2334+61, have been detected by ROSAT. Thus numerical simulations are desirable to tell the differences in these pulsars.

There is growing evidence that the optical emission of the spin-powered pulsars are of non-thermal origin. The ICS of the higher generation pairs discussed in this paper has a spectrum which could extend to as low as the optical band. However, the resonant ICS condition fails

in this regime, so that we could not present a plausible estimate of the optical luminosities without detailed numerical simulations. Thus whether or not the observed non-thermal optical emission is due to such ICS processes remains unclear.

Radio emission from pulsars is commonly believed to be of certain coherent origin owing to the very high brightness temperatures observed. Thus pair production, which can arise various plasma instabilities in the magnetospheres, is believed to be the essential condition of pulsar radio emission. Our full-polar cap cascade model presents multi-component pairs with different energies, which increases the possibilities of the “overtaking” two-stream instabilities that might account for pulsar radio emission. Such detailed models deserve constructing.

#### 4.4. Detailed comparisons with observations

It is worth presenting a closer comparison of our model predictions with the observations of some well-observed pulsars.

Crab and PSR B0540-69: Crab and its twin in the LMC are the youngest known pulsars. Both the ROSAT and ASCA observations show that they have very high luminosity radiation in X-rays, which are 1-2 orders of magnitude higher than our predictions. This leads one to suspect that there might be some more efficient X-ray emission mechanisms operating in these pulsars. However, our model could not be ruled out. We noticed that the luminosity data reported by BT97 and S98 are the values assuming isotropic emission of the X-rays. Thus the actual values should be much smaller if the radiation is strongly beamed. For example, these values could be down by an order of magnitude if one assumes the radiation is coming from 1 steradian solid angle. For Crab and PSR B0540-69, the strong non-thermal spectral features make us suspect its magnetospheric origin, and thus, the emission could be beamed.

Vela: Vela pulsar is actually weaker in X-rays than expected. It was not until 1993 when Ögelman, Finley & Zimmermann (1993) first discovered its weak pulsed X-ray emission with ROSAT. Its soft X-ray emission is dominated by a thermal component with the surface radius only 3-4km, which is much smaller than the conventional value, i.e. 10km. In fact, in BT97 and S98, the detected X-ray luminosities are much lower than the expected values according to their empirical relationships. Recent RXTE (2-30keV) observations (Strickman, Harding & deJager 1999) reveal an even lower luminosity in this band. Such a feature does not conflict with our model prediction, since what we predicted is an upper limit (see Table 3). An interesting discovery of Strickman, Harding & deJager (1999) is that although the RXTE spectrum of Peak 1 of this pulsar joins to the OSSE spectrum smoothly, the spectrum of Peak 2 does show the evidence of another component, which would extrapolate to within a factor of two of the optical spectrum. Detailed numerical simulations might be able to show whether the extra component is of ICS origin.

PSR B1509-58 and other high  $B$  pulsars: We have discussed the possible complications in high  $B$  pulsars. Our present predictions are not inconsistent with the observations. It is worth noticing that by adopting (83) rather than (77) to do the calculation (thus assuming ICS

branches do not pair produce), the prediction is nearly 2 order of magnitudes lower than the observations for PSR B1509-58. This indicates that the higher order ICS branches actually play an important role in high  $B$  pulsars.

Geminga, PSR B1055-52, and PSR B0656+14: these three middle-aged pulsars are the ones which have detailed spectral information, and are identified as “cooling pulsars”, which consist of a cooling thermal component and a non-thermal power law. As shown in Table 2, our model predictions show comparable luminosities of the non-thermal and full surface thermal components for these pulsars, and hence can well reproduce the observed features.

PSR 1929+10 and PSR 0950+08: As discussed in Sect.1, the spectral nature of these two old pulsars are still unclear, though they all probably have a hot polar cap thermal component. Since both the full surface temperature and the hot polar cap temperature are much lower in these pulsars, the ICS conversion efficiency should be considerably lower. Thus the non-thermal luminosity could be much lower than the upper limit we predicted. As a result, most probably, the thermal component from the hot polar cap may have comparable luminosity as the non-thermal component, so that such hot polar caps could be detectable. Though PSR 1929+10 is fitted by a single small area thermal component by Wang & Halpern (1997), it could be equally well fitted by a thermal polar cap plus a non-thermal component spectrum (BT97), which is just expected by our model. Future XMM observations on these two old pulsars will test our model predictions. As discussed in Sect.4.2, the thermal plus non-thermal feature of these two pulsars might be also adopted as a distinguishing criterion for the competing models.

Millisecond pulsars: as discussed above, our model prediction for the millisecond pulsars could be a feature to distinguish the rivaling models. For PSR J0437-4715 and PSR B1821-24, our model seems to have presented a qualitatively correct picture. The fact that a two component fit for PSR J0437-4715 requires a small-area thermal component actually supports our idea of the thermal origin of the pulsed soft X-rays from millisecond pulsars. We emphasize that the thermal feature we have predicted is only for the *pulsed* X-ray emission from millisecond pulsars. Another remark is that stronger multipole fields near the surface, if any, will make the polar cap model and the outer gap model indistinguishable since both models predict the non-thermal dominant feature.

We are grateful to the referee Werner Becker for his informative instructions and helpful advice, and Alex Muslimov for important discussions and useful comments.

## APPENDIX

## DERIVATION OF EQUATION (35)

The point of this appendix was first noted by Cheng & Ruderman (1977), and was adopted in WSL97. However, as shown below, a slightly different definition (i.e. A3, A4) makes (A9) an accurate relation rather than an asymptotic form for the relativistic cases.

Suppose the  $i$ th generation  $\gamma$ -ray  $\epsilon_i$  produce  $(i+1)$ -th generation pair with  $\gamma_{i+1} = \epsilon_i/2$  and pitch angle  $\theta_{\text{kB}}$ , then  $\gamma_{i+1}$  can be generally expressed as

$$\gamma_{i+1} = [1 + (p_{i+1,\parallel}/mc)^2 + 2nB']^{1/2}, \quad (\text{A1})$$

where  $n$  is the number of the Landau levels in the direction perpendicular to the field line. For  $n \gg 1$ , this could also be expressed classically as

$$\gamma_{i+1} = [1 + (p_{i+1,\parallel}/mc)^2 + (p_{i+1,\perp}/mc)^2]^{1/2}, \quad (\text{A2})$$

where  $p_{i+1,\parallel} = p_{i+1} \sin \theta_{\text{kB}}$  and  $p_{i+1,\perp} = p_{i+1} \cos \theta_{\text{kB}}$ . Define

$$\hat{\gamma}_{i+1,\parallel} = [1 + (p_{i+1,\parallel}/mc)^2]^{1/2} \quad (\text{A3})$$

and

$$\gamma_{i+1,\perp} = [1 + (p_{i+1,\perp}/mc)^2]^{1/2}, \quad (\text{A4})$$

we get

$$\gamma_{i+1}^2 = \hat{\gamma}_{i+1,\parallel}^2 + \gamma_{i+1,\perp}^2 - 1 \quad (\text{A5})$$

and

$$\cos^2 \theta_{\text{kB}} = \frac{\hat{\gamma}_{i+1,\parallel}^2 - 1}{\gamma_{i+1}^2 - 1}. \quad (\text{A6})$$

This is a little bit different from Cheng & Ruderman (1977) who defined  $\hat{\gamma}_{i+1,\parallel} = p_{i+1,\parallel}/mc$  and  $\gamma_{i+1,\perp} = p_{i+1,\perp}/mc$ . Note  $\hat{\gamma}_{i+1,\parallel}$  is not the parallel energy of the particle we are interested in, since when the particle emits the SR photons, it will receive a recoil force so that its momentum is usually changed.

Now define a Lorentz frame with  $\gamma_{i+1,\parallel}$  (different from  $\hat{\gamma}_{i+1,\parallel}$ ) in which only perpendicular momentum is left. In such a co-moving frame, the emission of SR photons will usually bring no recoil to the particle in the parallel direction as long as the particle emits photons in the direction perpendicular to the magnetic field, i.e., the particle is in high enough Landau levels. This is true in most cases we discussed in this paper. (Note when the particle is in a very low Landau state, above conclusion is not necessarily true, since the SR photons will be emitted in random directions.) Thus such a Lorentz factor is identical to the real Lorentz factor of the particle after it emits all its perpendicular energy via SR. A handy Lorentz transformation leads to the relation

$$\cos^2 \theta_{\text{kB}} = \frac{1 - \gamma_{i+1,\parallel}^{-2}}{1 - \hat{\gamma}_{i+1,\parallel}^{-2}}. \quad (\text{A7})$$

Compare [A6] with [A7], we finally get

$$\gamma_{i+1,\parallel}^2 = \frac{\gamma_{i+1}^2}{\gamma_{i+1}^2 - \hat{\gamma}_{i+1,\parallel}^2 + 1} \quad (\text{A8})$$

or

$$\gamma_{i+1,\parallel} = \frac{\gamma_{i+1}}{\gamma_{i+1,\perp}} = \frac{\gamma_{i+1}}{[1 + (\gamma_{i+1}^2 - 1) \sin^2 \theta_{\text{kB}}]^{1/2}}, \quad (\text{A9})$$

which is the equation (35) in the text.

## REFERENCES

- Alpar, M.A., Anderson, P.W., Pines, D., & Shaham, J. 1984, ApJ, 278, 791  
Arons, J. 1981, ApJ, 248, 1099  
— 1983, ApJ, 266, 215  
Arons, J., & Scharlemann, E.T. 1979, ApJ, 231, 854  
Arons, J., & Tavani, M. 1993, ApJ, 403, 249  
Baring, M.G. 1988, MNRAS, 235, 51  
Baring, M.G., & Harding, A.K. 1999, ApJ, in preparation  
Becker, W., & Trümper, J. 1993, Nature, 365, 528  
— 1997, A&A, 326, 682, updated version: [http://www.xray.mpe.mpg.de/~web/bt97/bt97\\_update.html](http://www.xray.mpe.mpg.de/~web/bt97/bt97_update.html) (BT97)  
— 1999, A&A, 341, 803  
Cheng, A.F., & Ruderman, M.A. 1977, ApJ, 216, 865  
Cheng, K.S., Gil, J. & Zhang, L. 1998, ApJ, 493, L35 (CGZ98)  
Cheng, K.S., Ho, C. & Ruderman, M.A. 1986a, ApJ, 300, 500  
Cheng, K.S., Ho, C. & Ruderman, M.A. 1986b, ApJ, 300, 522  
Cheng, K.S., & Zhang, L. 1999, ApJ, 515, 337 (CZ99)  
Daugherty, J.K., & Harding, A.K. 1982, ApJ, 252, 337  
— 1983, ApJ, 273, 761  
— 1989, ApJ, 336, 861  
— 1994, ApJ, 429, 325  
— 1996, ApJ, 458, 278 (DH96)  
Daugherty, J.K., & Lerche, I. 1975, ApSS, 38, 437  
Dermer, C.D. 1990, ApJ, 360, 214  
Deshpande, A.A., & Rankin, J.M. 1999, ApJ, 524, 1008  
Erber, T. 1966, Rev. Mod. Phys., 38, 626  
Goldreich, P., & Julian, W.H. 1969, ApJ, 157, 869  
Gonthier, P.L. & Harding, A.K. 1994, ApJ, 425, 767  
Grelvedinger, C., et al. 1996, ApJ, 465, L35  
Halpern, J.P., Martin, C., & Marshall, H.L. 1996, ApJ, 462, 908  
Halpern, J.P., & Wang, F.Y.-H. 1997, ApJ, 477, 905  
Hardee, P.E. 1977, ApJ, 216, 873

- Harding, A.K. 1981, *ApJ*, 245, 267  
 —. 1991, *Phys. Rep.*, 206(6), 327  
 Harding, A.K., Baring, M.G., & Gonthier, P.L. 1997, *ApJ*, 476, 246  
 Harding, A.K. & Daugherty, J.K. 1999, in *Proc. 3rd Integral Workshop*, in press  
 Harding, A.K., & Muslimov, A.G. 1998, *ApJ*, 508, 328 (HM98)  
 Harding, A.K., Ozernoy, L.M., & Usov, V.V. 1993, *MNRAS*, 265, 921  
 Harding, A.K., & Preece, R. 1987, *ApJ*, 319, 939  
 Harding, A.K., Tadamaru, E., & Esposito, L.W. 1978, *ApJ*, 225, 226  
 Jones, P.B. 1985, *Phys. Rev. Lett.*, 55, 1338  
 —. 1986, *MNRAS*, 218, 477  
 Kardashev, N.S., Mitrofanov, I.G., & Novikov, I.D. 1984, *AZh*, 61, 1113 (English transl. *Soviet Astron.*, 28, 651)  
 Kaspi, V.M., Lackey, J.R., Mattox, J., Manchester, R.N., Bailes, M., & Pace, R. 1999, *ApJ*, in press (astro-ph/9906373)  
 Lu, T., & Shi, T.Y. 1990, *A&A*, 231, L7  
 Lu, T., Wei, D.M., & Song, L.M. 1994, *A&A*, 290, 815 (LWS94)  
 Manchester, R.N., & Taylor, J.H. 1977, *Pulsars* (San Francisco: Freeman)  
 Michel, F.C. 1991, *Theory of Neutron Star Magnetospheres* (Chicago: Univ. Chicago Press)  
 Muslimov, A.G., & Harding, A.K. 1997, *ApJ*, 485, 735  
 Muslimov, A.G., & Tsygan, A.I. 1992, *MNRAS*, 255, 61  
 Nomoto, K., & Tsuruta, S. 1987, *ApJ*, 312, 711  
 Neuhauser, D., Langanke, K., & Koonin, S.E. 1986, *Phys. Rev.*, A33, 2084  
 Neuhauser, D., Koonin, S.E., & Langanke, K. 1987, *Phys. Rev.*, A36, 4163  
 Ögelman, H., Finley, J.P., & Zimmermann, H.U. 1993, *Nature*, 361, 136  
 Paczynski, B. 1990, *ApJ*, 348, 485  
 Romani, R.W. 1996, *ApJ*, 470, 469  
 Romani, R.W. & Yadigaroglu, I.-A. 1995, *ApJ*, 438, 314  
 Rudak, B. & Dyks, J. 1999, *MNRAS*, 303, 477  
 Ruderman, M.A., & Sutherland, P.G. 1975, *ApJ*, 196, 51 (RS75)  
 Saito, Y. 1998, PhD thesis, Univ. of Tokyo (S98)  
 Saito, Y., Kawai, N., Kamae, T., & Shibata, S. 1997, in: N.Shibazaki, N.Kawai, S.Shibata & T.Kifune (eds), *Neutron Stars and Pulsars: thirty years after discovery*, Tokyo: Universal Academy Press, 295  
 Schaab, C., Sedrakian, A., Weber, F., & Weigel, M.K. 1999, *A&A*, 346, 465  
 Shapiro, S.L., & Teukolsky, S.A. 1983, *Black Holes, White Dwarfs, and Neutron Stars: the physics of compact objects*, John Wiley & Sons  
 Shibazaki, N., & Lamb, F. 1988, *ApJ*, 346, 808  
 Strickman, M.S., Harding, A.K. & deJager, O.C. 1999, *ApJ*, 524, 373  
 Sturmer, S.J. 1995, *ApJ*, 446, 292  
 Sturmer, S.J., & Dermer, C.D. 1994, *ApJ*, 420, L79  
 Sturmer, S.J., Dermer, C.D., & Michel, F.C. 1995, *ApJ*, 445, 736 (SDM95)  
 Taylor, J.H., Manchester, R.N., Lyne, A.G., & Camilo, F. 1995, extended work of Taylor, Manchester & Lyne, 1993, *ApJS*, 88, 529, latest version from the Princeton pulsar archives  
 Thompson, D.J., Bailes, M., Bertsch, D.J., Cordes, J., et al. 1999, *ApJ*, 516, 297  
 Thompson, D.J., Harding, A.K., Hermsen, W., & Ulmer, M.P. 1997, in C.D. Dermer, M.S. Strickman, & J.D. Kurfess (eds.), *Proc. Fourth Compton Symposium*, AIP Conf. Proc. 410, 39  
 Usov, V.V., & Melrose, D.B. 1995, *Aust. J. Phys.*, 48, 571  
 —. 1996, *ApJ*, 464, 306  
 Van Riper, K.A., & Lamb, D.Q. 1981, *ApJ*, 244, L13  
 Vivekanand, M., & Joshi, B.C. 1999, *ApJ*, 515, 398  
 Wang, F.Y.-H., & Halpern, J.P. 1997, *ApJ*, 482, L159  
 Wang, F.Y.-H., Ruderman, M., Halpern, J.P. & Zhu, T. 1998, *ApJ*, 498, 373  
 Wasserman, I., & Shapiro, S.L. 1983, *ApJ*, 265, 1036  
 Wei, D.M., Song, L.M., & Lu, T. 1997, *A&A*, 323, 98 (WSL97)  
 Xia, X.Y., Qiao, G.J., Wu, X.J., & Hou, Y.Q. 1985, *A&A*, 152, 93  
 Zavlin, V.E., & Pavlov, G.G. 1998, *A&A*, 329, 583  
 Zhang, B., & Harding, A.K. 1999, in *Proc. Fifth Compton Symposium* (Portsmouth, NH), AIP Conf. Proc., in press  
 Zhang, B., Harding, A.K., & Muslimov, A.G. 1999, *ApJL*, submitted  
 Zhang, B., & Qiao, G.J. 1996, *A&A*, 310, 135  
 Zhang, B., Qiao, G.J., & Han, J.L. 1997b, *ApJ*, 491, 891  
 Zhang, B., Qiao, G.J., Lin, W.P., & Han, J.L. 1997a, *ApJ*, 478, 313  
 Zhang, L., & Cheng, K.S. 1997, *ApJ*, 487, 370  
 Zhao, Y.H., Lu, T., Huang, K.L., Lu, J.L., & Peng, Q.H. 1989, *A&A*, 223, 147  
 Zheng, Z., Zhang, B., & Qiao, G.J. 1998, *A&A*, 334, L49

TABLE A1

Broad-band high energy luminosities (above 1eV, most luminosity contributions are from the band above 100KeV, thus denoted as  $L_\gamma$ ) observed (Thompson et al. 1999) and expected. The luminosity for PSR B1046-58 is adopted by that above 400 MeV, following Kaspi et al. (1999). Pulsar data are taken from Taylor et al. (1995). ‘o’ denotes observed value, ‘m’ denotes model prediction, ‘f’ denotes the full-cascade model discussed in this paper, and ‘c’ denotes the canonical CR-SR cascade model.

Pulsars	P(ms)	Log B(G)	$L_{sd}$	$L_\gamma(o)$	$L_\gamma(m,f)$	$L_\gamma(m,c)$
B0531 + 21	33.40	12.88	38.65	35.70	35.54	34.94
B0833 - 45	89.29	12.83	36.84	34.38	34.71	34.22
B0633 + 17	237.09	12.51	34.51	32.98	33.56	33.38
B1706 - 44	102.45	12.79	36.53	34.84	34.57	34.12
B1509 - 58	150.23	13.49	37.25	35.21	34.85	32.33
B1951 + 32	39.53	11.99	36.57	34.40	34.64	34.58
B1055 - 52	197.10	12.34	34.48	33.79	33.56	33.45
B1046 - 58	123.65	12.84	36.30	34.34	34.46	33.96

TABLE A2

Model parameters of the spin-powered X-ray pulsars. Pulsar data are taken from Taylor et al. (1995). The 4th column ‘regime’ denotes the regime of the accelerator: ‘I’ indicates the unsaturated case, while ‘II’ indicates the saturated case. Normal pulsars and millisecond pulsars are grouped separately.

Pulsars	$P(ms)$	$\log B(G)$	regime	$f$	$\kappa_{SR}$	$\kappa_{ICS}$	$\zeta_{SR}$	$\zeta_{ICS}$	$\eta_\perp$	$\eta_\parallel$
B0531 + 21	33.40	12.88	I	0.00010	$6.25 \times 10^{-2}$	$9.66 \times 10^{-3}$	3.44	2.46	0.669	0.331
B0833 - 45	89.29	12.83	I	0.00019	$6.25 \times 10^{-2}$	$7.64 \times 10^{-3}$	3.21	2.26	0.704	0.296
J1811 - 1926	64.66	13.11	I	0.00011	$6.25 \times 10^{-2}$	$2.58 \times 10^{-2}$	3.41	2.83	0.485	0.515
J1617 - 5055	69.33	12.80	I	0.00017	$6.25 \times 10^{-2}$	$6.71 \times 10^{-3}$	3.25	2.25	0.722	0.278
B0633 + 17	237.09	12.51	II	0.00042	$6.25 \times 10^{-2}$	$1.74 \times 10^{-3}$	2.62	1.71	0.856	0.144
B1706 - 44	102.45	12.79	I	0.00021	$6.25 \times 10^{-2}$	$6.56 \times 10^{-3}$	3.16	2.19	0.725	0.275
B1509 - 58	150.66	13.49	I	0.00011	$6.25 \times 10^{-2}$	$9.68 \times 10^{-2}$	3.42	3.87	0.182	0.818
B1951 + 32	39.53	11.99	I	0.00035	$6.25 \times 10^{-2}$	$1.62 \times 10^{-4}$	2.97	1.63	0.956	0.044
B1046 - 58	123.65	12.84	I	0.00022	$6.25 \times 10^{-2}$	$8.07 \times 10^{-3}$	3.15	2.24	0.696	0.304
B1259 - 63	47.76	11.82	I	0.00049	$6.25 \times 10^{-2}$	$7.43 \times 10^{-5}$	2.85	1.54	0.970	0.030
J0537 - 6906	16.11	12.26	I	0.00015	$6.25 \times 10^{-2}$	$5.94 \times 10^{-4}$	3.30	1.86	0.916	0.084
B1823 - 13	101.45	12.75	I	0.00023	$6.25 \times 10^{-2}$	$5.26 \times 10^{-3}$	3.14	2.13	0.753	0.247
B1800 - 21	133.61	12.93	I	0.00021	$6.25 \times 10^{-2}$	$1.20 \times 10^{-2}$	3.18	2.36	0.635	0.365
B1929 + 10	226.52	12.02	II	0.00042	$6.25 \times 10^{-2}$	$1.50 \times 10^{-4}$	2.21	1.38	0.958	0.042
B0656 + 14	384.89	12.97	II	0.00026	$6.25 \times 10^{-2}$	$1.34 \times 10^{-2}$	2.70	2.09	0.615	0.385
B0540 - 69	50.37	13.00	I	0.00011	$6.25 \times 10^{-2}$	$1.59 \times 10^{-2}$	3.41	2.61	0.583	0.417
J1105 - 6107	63.19	12.31	I	0.00031	$6.25 \times 10^{-2}$	$7.01 \times 10^{-4}$	3.03	1.77	0.908	0.092
B0950 + 08	253.07	11.69	II	0.00024	$6.25 \times 10^{-2}$	$4.39 \times 10^{-5}$	1.55	1.15	0.977	0.023
B1610 - 50	231.60	13.33	I	0.00017	$6.25 \times 10^{-2}$	$5.83 \times 10^{-2}$	3.25	3.20	0.295	0.705
J0538 + 2817	143.16	12.16	II	0.00070	$6.25 \times 10^{-2}$	$3.56 \times 10^{-4}$	2.65	1.58	0.935	0.065
B1055 - 52	197.10	12.34	II	0.00050	$6.25 \times 10^{-2}$	$7.66 \times 10^{-4}$	2.59	1.61	0.904	0.096
B0355 + 54	156.38	12.22	II	0.00064	$6.25 \times 10^{-2}$	$4.65 \times 10^{-4}$	2.65	1.59	0.925	0.075
B2334 + 61	495.28	13.29	II	0.00020	$6.25 \times 10^{-2}$	$4.96 \times 10^{-2}$	2.81	2.67	0.334	0.666
B0823 + 26	530.66	12.29	II	0.00012	$6.25 \times 10^{-2}$	$7.41 \times 10^{-4}$	1.59	1.23	0.906	0.094
B1853 + 01	267.40	13.18	II	0.00038	$6.25 \times 10^{-2}$	$3.30 \times 10^{-2}$	3.11	2.71	0.430	0.570
J0437 - 4715	5.75	9.06	II	0.0081	$9.38 \times 10^{-2}$	$5.74 \times 10^{-10}$	1.49	1.05	0.9999	0.0001
B1937 + 21	1.55	8.90	II	0.0415	$9.38 \times 10^{-2}$	$7.22 \times 10^{-10}$	2.50	1.17	0.9999	0.0001
B1821 - 24	3.05	9.65	II	0.0216	$9.38 \times 10^{-2}$	$2.46 \times 10^{-8}$	2.74	1.23	0.9996	0.0004
J2124 - 3358	4.93	8.67	II	0.0070	$9.38 \times 10^{-2}$	$3.87 \times 10^{-11}$	1.05	1.01	1.0000	0.0000
B1957 + 20	1.60	8.52	II	0.0367	$9.38 \times 10^{-2}$	$9.66 \times 10^{-11}$	2.05	1.11	1.0000	0.0000
J1024 - 0719	5.18	8.79	II	0.0074	$9.38 \times 10^{-2}$	$9.26 \times 10^{-11}$	1.19	1.02	1.0000	0.0000
J1744 - 1134	4.07	8.58	II	0.0091	$9.38 \times 10^{-2}$	$3.13 \times 10^{-11}$	1.14	1.01	1.0000	0.0000
J1012 + 5307	5.25	8.74	II	0.0068	$9.38 \times 10^{-2}$	$5.83 \times 10^{-11}$	1.09	1.01	1.0000	0.0000
J0218 + 4232	2.32	8.94	II	0.0263	$9.38 \times 10^{-2}$	$7.42 \times 10^{-10}$	2.21	1.14	0.9999	0.0001
J0751 + 1807	3.47	8.53	II	0.0116	$9.38 \times 10^{-2}$	$3.17 \times 10^{-11}$	1.26	1.03	1.0000	0.0000

TABLE A3

X-ray luminosities observed and expected in the ROSAT band and ASCA bands. ROSAT data follow BT97, and ASCA data follow S98. The middle 6 columns are for the ROSAT band, and the right 3 columns are for the ASCA band. ‘o’ denotes observed value and ‘m’ denotes model prediction. the superscript ‘tot’ indicates total luminosity detected, ‘pul’ indicates the luminosity of the pulsed portion, ‘nth’ denotes non-thermal, and ‘th1’ and ‘th2’ denote thermal emission of full surface and polar cap, respectively.

Pulsars	$L_{sd}$	ROSAT band						ASCA band		
		$L_x^{tot}(o)$	$L_x^{pul}(o)$	$L_x^{th1}(m)$	$L_x^{th2}(m)$	$L_x^{nth}(m)$	$L_x^{tot}(m)$	$L_x^{tot}(o)$	$L_x^{pul}(o)$	$L_x(m)$
B0531 + 21	38.65	35.98	35.85	32.49	$\gtrsim$ 31.55	< 34.25	< 34.26	37.02	35.83	< 34.83
B0833 - 45	36.84	32.70	31.7	32.96	$\gtrsim$ 30.98	< 33.35	< 33.50	33.28	< 31.83	< 33.96
J1811 - 1926	37.97			32.45	$\gtrsim$ 31.24	< 34.23	< 34.24			< 34.63
J1617 - 5055	37.22			32.17	$\gtrsim$ 31.11	< 33.73	< 33.74			< 34.21
B0633 + 17	34.51	31.10	30.62	31.24	$\gtrsim$ 30.18	< 31.72	< 31.86	29.79	29.56	$\gtrsim$ 32.33
B1706 - 44	36.53	33.15		32.03	$\gtrsim$ 30.89	< 33.46	< 33.48	32.83	< 32.73	< 33.91
B1509 - 58	37.25	34.29	34.10	32.45	$\gtrsim$ 30.88	< 33.74	< 33.76	34.60	34.80	< 34.34
B1951 + 32	36.57	33.44		31.72	$\gtrsim$ 31.19	$\gtrsim$ 32.18	$\gtrsim$ 32.34	33.79	< 32.93	$\gtrsim$ 32.78
B1046 - 58	36.30	$\leq$ 32.11		32.01	$\gtrsim$ 30.80	< 33.34	< 33.36	32.96	< 32.78	< 33.80
B1259 - 63	35.92	32.95		31.00	$\gtrsim$ 31.04	$\gtrsim$ 31.92	$\gtrsim$ 32.02			$\gtrsim$ 32.53
J0537 - 6906	38.68			32.25	$\gtrsim$ 31.78	< 34.24	< 34.25			$\gtrsim$ 34.45
B1823 - 13	36.45	33.39		32.00	$\gtrsim$ 30.88	< 33.45	< 33.46			$\gtrsim$ 33.83
B1800 - 21	36.35	33.06		32.05	$\gtrsim$ 30.78	< 33.31	< 33.33			< 33.80
B1929 + 10	33.60	30.00	29.5	29.07	$\gtrsim$ 29.72	< 31.63	< 31.64	30.08	< 29.92	< 31.70
B0656 + 14	34.58	32.98	32.15	31.86	$\gtrsim$ 29.95	< 32.24	< 32.39		< 31.23	< 32.83
B0540 - 69	38.17	36.21	36.1	32.44	$\gtrsim$ 31.35	< 33.98	< 33.99	36.92	36.11	< 34.58
J1105 - 6107	36.39			31.81	$\gtrsim$ 31.02	< 33.34	< 33.35			$\gtrsim$ 33.41
B0950 + 08	32.75	29.35		27.56	$\gtrsim$ 28.88	< 30.28	< 30.30	29.00	< 29.00	< 30.84
B1610 - 50	36.19			32.18	$\gtrsim$ 30.59	< 33.59	< 33.61	34.36	< 34.36	< 34.12
J0538 + 2817	34.69	32.74		30.46	$\gtrsim$ 30.55	< 31.81	< 31.85			$\gtrsim$ 32.42
B1055 - 52	34.48	33.42	32.57	31.86	$\gtrsim$ 30.26	< 31.49	< 32.03	30.45	< 30.43	$\gtrsim$ 32.10
B0355 + 54	34.66	31.96		30.54	$\gtrsim$ 30.48	< 31.82	< 31.86			$\gtrsim$ 32.43
B2334 + 61	34.80	31.86		31.89	$\gtrsim$ 29.93	< 32.15	< 32.34			< 32.75
B0823 + 26	32.66	29.83		28.67	$\gtrsim$ 28.45	< 30.74	< 30.75			$\gtrsim$ 31.32
B1853 + 01	35.63			32.01	$\gtrsim$ 30.69	< 32.83	< 32.89	33.15	< 33.15	< 33.33
J0437 - 4715	34.07	30.86	30.3	23.64	$\gtrsim$ 31.30	$\sim$ 29.82	$\gtrsim$ 31.31	30.08	< 30.08	$\sim$ 30.06
B1937 + 21	36.03	$\leq$ 32.10		25.27	$\gtrsim$ 33.13	$\sim$ 31.22	$\gtrsim$ 33.13			$\sim$ 31.46
B1821 - 24	36.35	33.24		27.09	$\gtrsim$ 32.93	$\sim$ 31.54	$\gtrsim$ 32.95	33.81	32.97	$\sim$ 31.77
J2124 - 3358	33.55	30.35	29.8	22.33	$\gtrsim$ 30.99	$\sim$ 29.49	$\gtrsim$ 31.01			$\sim$ 29.74
B1957 + 20	35.20	31.93		23.70	$\gtrsim$ 32.66	$\sim$ 30.78	$\gtrsim$ 32.67			$\sim$ 31.03
J1024 - 0719	33.71	29.48		22.73	$\gtrsim$ 31.09	$\sim$ 29.59	$\gtrsim$ 31.10			$\sim$ 29.83
J1744 - 1134	33.70	29.30		22.30	$\gtrsim$ 31.20	$\sim$ 29.54	$\gtrsim$ 31.21			$\sim$ 29.78
J1012 + 5307	33.58	30.20		22.50	$\gtrsim$ 30.99	$\sim$ 29.52	$\gtrsim$ 31.00			$\sim$ 29.77
J0218 + 4232	35.40	32.75		24.72	$\gtrsim$ 32.57	$\sim$ 30.96	$\gtrsim$ 32.58			$\sim$ 31.20
J0751 + 1807	33.88	31.60		22.37	$\gtrsim$ 31.41	$\sim$ 29.60	$\gtrsim$ 31.42			$\sim$ 29.85